

**Implementation of multiphase piezoelectric composites energy harvester on aircraft wingbox structure with fuel saving evaluation.**

AKBAR, Mahesa and CURIEL-SOSA, JL

Available from Sheffield Hallam University Research Archive (SHURA) at:

<https://shura.shu.ac.uk/34040/>

---

This document is the Accepted Version [AM]

**Citation:**

AKBAR, Mahesa and CURIEL-SOSA, JL (2018). Implementation of multiphase piezoelectric composites energy harvester on aircraft wingbox structure with fuel saving evaluation. *Composite Structures*, 202, 1000-1020. [Article]

---

**Copyright and re-use policy**

See <http://shura.shu.ac.uk/information.html>

# Implementation of Multiphase Piezoelectric Composites Energy Harvester on Aircraft Wingbox Structure with Fuel Saving Evaluation

M. Akbar\*, J.L. Curiel-Sosa

*Department of Mechanical Engineering, Computer-Aided Aerospace and Mechanical Engineering Research Group (CA2M), The University of Sheffield, The Portobello Centre, Sheffield, S1 4ET, United Kingdom*

---

## Abstract

The multiphase composite with active structural fiber (ASF) has proven able to provide better optimization between actuating and load bearing capability compared to a pure piezoelectric material. In this paper, the multiphase composite application is further extended for energy harvesting purpose. The Double-Inclusion model combined with Mori-Tanaka method is implemented in a computational code to estimate the effective electro-elastic properties of the multiphase composite. The effective composite properties obtained via the present code are in good agreement with the analytical, experimental and finite element results. The multiphase composite with different composition is applied to a typical jet aircraft wingbox with 14.5 m halfspan. The energy harvesting evaluation by means of hybrid FEM/analytical piezoelectric energy harvester model is presented. A new procedure to investigate the trade-off between the aircraft weight, the fuel saving and the energy harvested is developed. The results pointed out that the equivalent fuel saved from the power generated by the wingbox is more than enough for 1 hour Auxiliary Power Unit (APU) operation.

*Keywords:* Piezoelectric Energy Harvester, Active Structural Fiber (ASF), Multiphase Composite, Double-Inclusion Model, Aircraft Wingbox, Fuel Saving

---

## 1. Introduction

The multifunctional material system has attracted significant attention in the past decade. Christodoulou and Venables [1] established the first classification of the Multifunctional Material Systems. The review by Gibson [2] noted a significant growth of publication related to this topic in its earlier years, during the 2000-2009 period. Ferreira et al. [3] stated that the structural capability along with other functions, i.e., self-healing, actuation, shape changing, power generation and storage, are required in the future multifunctional material systems. In a survey by Toprak and Tigli [4], almost 1000 articles related to piezoelectric energy harvesting were published during the 2013-2014 period. In the present work, a study on the piezoelectric-based energy harvesting from structural vibration is focused.

One of the earliest implementations in piezoelectric energy harvesting was done by Anton and Inman [5]. The piezoelectric patches embedded on a remote control aircraft proven able to harvest the energy from structural vibration during the flight. Since then, numerous studies have been conducted on the energy harvesting potential via piezoelectric structural vibration. Most notably, the series of work by Erturk and Inman [6–8] has influenced a large number of developments on the piezoelectric energy harvester model. Erturk and Inman in [7] developed the first mathematical model of cantilevered piezoelectric energy harvester under base excitation.

The extension of the base excitation model is seen in the research on the piezoaeroelastic energy harvester model. Various models have been developed from the two-degree of freedoms (2DoF) airfoil until the planar lifting surface model [9–14]. The reviews in [15–18] provided discussions on the state-of-the-art of the piezoaeroelastic energy harvesting. However, most of the models involved resonance effect, i.e., Vortex-Induced Vibration, and instability condi-

---

\*Corresponding author

*Email addresses:* makbar2@sheffield.ac.uk (M. Akbar), j.curiel-sosa@sheffield.ac.uk (J.L. Curiel-Sosa)

*URL:* <http://www.jlcurielsosa.org> (J.L. Curiel-Sosa)

tion, i.e., flutter as reviewed in [17].

In contrast with the extensive development of the piezoaeroelastic model, the evaluation of the normal operating condition, i.e., low wind speed on civil structure, cruise/gust loads on aircraft, only received small attention. In the aircraft related field, to the authors' knowledge, there are just a few articles proposed energy harvester models under gust load. Discrete gust load models are proposed in [19–21]. Meanwhile, the model for random gust loads was developed by Tsushima and Su in [22] and further extended in [23]. In addition, the model for post-flutter speed limit cycle oscillation (LCO) is proposed in [24].

Akbar and Curiel-Sosa [25] proposed the hybrid analytical/numerical scheme for dynamic bending condition which implemented in a cruise scenario. The extension of the hybrid scheme can be seen in [26]. Advance numerical method, i.e., isogeometric analysis, is coupled with the scheme and provides better shear locking resistance. Shear locking itself commonly occurs in thin shells and leads to a poor accuracy [27, 28]. The hybrid scheme also shows faster computational time compared to a full electromechanical finite element model [26]. Hence, it is considered a good alternative in the early design stage.

However, a crucial issue was noticed in the investigation of the wingbox structure in [25]. The replacement of the original material by the piezoelectric material resulted in a massive increase in the structural weight. Therefore, to address this issue, a novel implementation of the multiphase piezoelectric composite for energy harvesting purpose is proposed herein. The multiphase composite proposed by Lin and Sodano in [29] is adopted.

Lin and Sodano first introduced a concept of active structural fiber (ASF) in [30]. The ASF consisted of a core fiber and piezoelectric shell. The core fiber dedicated to giving more structural capability, i.e., load-bearing function. In contrast, the piezoelectric shell provides more functions related to electro-mechanical coupling. The fabrication and experimental test of the ASF are explained in [31, 32]. Furthermore, the ASF is embedded in a matrix to construct the multiphase composite model in [29].

The Double-Inclusion model was proposed in [29] to estimate the effective electro-elastic properties of the multiphase composite. The model was well validated with FEM simulation. The Double-Inclusion model initially derived for elastic material by Hori and Nemat-Nasser in [33] and further improved by

Dunn and Ledbetter [34]. In order to incorporate the full electro-elastic properties, the piezoelectric analog of the Eshelby's tensor [35] was introduced to the Double-Inclusion model in [29].

Eshelby's tensor [36] itself was initially established for elastic material and further developed to the homogenization scheme, i.e., effective medium approximation, by Hashin [37] and Mori-Tanaka [38]. One of the most well-known and the simplest homogenization method is the rule of mixture. The implementation of the Eshelby's tensor with Mori-Tanaka method provides greater accuracy than the rule of mixture for large volume fraction [39].

Chan and Unsworth [40] derived one of the earliest analytical models to homogenize the properties of the single piezoelectric fiber composite. Dunn and Taya [41] implemented the piezoelectric Eshelby tensor with various homogenization scheme, i.e., dilute model, Mori-Tanaka method, self-consistent model, to predict the properties of single piezoelectric fiber composites. Their results were compared with the experimental data of Chan and Unsworth [40]. It was found that best comparison with the experiment's is provided by the Mori-Tanaka method. Odegard in [42] also found that The Mori-Tanaka method also gives the closest comparison with the FEM results.

Other related works with the multiphase piezoelectric composite can be found in the development of the multi-inclusion piezoelectric composite models in [43–45] and the multiphase magneto-electro-elastic composite model in [46–48]. The interested reader also referred to a review article in [49] discussed various works on the inclusion model.

Despite the fact that the multiphase piezoelectric provide better multifunctional capability [29, 50], the implementation of energy harvesting structure is not found in the literature. In the present work, for the first time, the multiphase piezoelectric composite is applied to the energy harvesting structure. Furthermore, the Double-Inclusion model combined with Mori-Tanaka method is used to obtain a better accuracy of the effective composite properties. A new implementation of the multiphase composite energy harvester to a jet transport aircraft wingbox is performed. A novel procedure to evaluate the weight and energy trade-off due to the energy harvesting structure is developed. The mathematical models, evaluation procedures, validation and implementation results are explained in the following sections.

## 2. Mathematical Model

In this paper, the multiphase composite with electro-elastic constitutive matrix is concerned. The constitutive matrix of piezoelectric material is adopted to the multiphase composite. Two forms of the constitutive matrix, i.e., stress-charge, strain-charge, are used. The stress-charge form is mainly used in The Double-Inclusion formulation. While the strain-charge form is applied in the energy harvester model. Based on the IEEE standard on piezoelectricity [51], the stress-charge form is written as

$$\mathbf{E}_{iJMn} = \begin{bmatrix} C_{11} & C_{12} & C_{13} & 0 & 0 & 0 & 0 & 0 & -e_{31} \\ C_{12} & C_{11} & C_{13} & 0 & 0 & 0 & 0 & 0 & -e_{31} \\ C_{13} & C_{13} & C_{33} & 0 & 0 & 0 & 0 & 0 & -e_{33} \\ 0 & 0 & 0 & C_{44} & 0 & 0 & 0 & -e_{15} & 0 \\ 0 & 0 & 0 & 0 & C_{44} & 0 & -e_{15} & 0 & 0 \\ 0 & 0 & 0 & 0 & 0 & C_{66} & 0 & 0 & 0 \\ 0 & 0 & 0 & 0 & e_{15} & 0 & \varepsilon_{11}^S & 0 & 0 \\ 0 & 0 & 0 & e_{15} & 0 & 0 & 0 & \varepsilon_{11}^S & 0 \\ e_{31} & e_{31} & e_{33} & 0 & 0 & 0 & 0 & 0 & \varepsilon_{33}^S \end{bmatrix} \quad (1)$$

and the strain-charge form is expressed as

$$\mathbf{F}_{AbiJ} = \begin{bmatrix} S_{11} & S_{12} & S_{13} & 0 & 0 & 0 & 0 & 0 & d_{31} \\ S_{12} & S_{11} & S_{13} & 0 & 0 & 0 & 0 & 0 & d_{31} \\ S_{13} & S_{13} & S_{33} & 0 & 0 & 0 & 0 & 0 & d_{33} \\ 0 & 0 & 0 & S_{44} & 0 & 0 & 0 & d_{15} & 0 \\ 0 & 0 & 0 & 0 & S_{44} & 0 & d_{15} & 0 & 0 \\ 0 & 0 & 0 & 0 & 0 & S_{66} & 0 & 0 & 0 \\ 0 & 0 & 0 & 0 & d_{15} & 0 & \varepsilon_{11}^T & 0 & 0 \\ 0 & 0 & 0 & d_{15} & 0 & 0 & 0 & \varepsilon_{11}^T & 0 \\ d_{31} & d_{31} & d_{33} & 0 & 0 & 0 & 0 & 0 & \varepsilon_{33}^T \end{bmatrix} \quad (2)$$

In Equations (1) and (2), the symmetries due to orthotropic, i.e.,  $C_{11} = C_{22}$ ,  $d_{31} = d_{32}$ , etc., are directly applied. In a more compact form, Equations (1) and (2) are written as

$$\mathbf{E}_{iJMn} = \begin{bmatrix} \mathbf{C} & -\mathbf{e}^t \\ (6 \times 6) & (6 \times 3) \\ \mathbf{e} & \varepsilon^S \\ (3 \times 6) & (3 \times 3) \end{bmatrix} \quad (3)$$

$$\mathbf{F}_{AbiJ} = \begin{bmatrix} \mathbf{S} & \mathbf{d}^t \\ (6 \times 6) & (6 \times 3) \\ \mathbf{d} & \varepsilon^T \\ (3 \times 6) & (3 \times 3) \end{bmatrix} \quad (4)$$

$\mathbf{C}$  and  $\mathbf{S}$  are the stiffness/elasticity matrix and the compliance matrix, respectively. The piezoelectric coupling constants in stress-charge and strain-charge forms are defined by  $\mathbf{e}$  and  $\mathbf{d}$ . The piezoelectric constant,  $\mathbf{d}$  also called as the charge constant. The dielectric permittivity in stress-charge and strain-charge forms are represented by  $\varepsilon^S$  and  $\varepsilon^T$ . The dielectric permittivity of the material often written as relative permittivity, non-dimensionalised by the vacuum permittivity,  $\varepsilon_0 = 8.85 \times 10^{-12}$  F/m.

The transformations between the stress-charge form and strain-charge form are shown as follows

$$\begin{aligned} \mathbf{C} &= \mathbf{S}^{-1} \\ \mathbf{e} &= \mathbf{d} \mathbf{S}^{-1} \\ \varepsilon^S &= \varepsilon^T - \mathbf{d} \mathbf{S}^{-1} \mathbf{d}^t \end{aligned} \quad (5)$$

### 2.1. The Double Inclusion Model

The illustration of the piezoelectric shell embedded in a carbon fiber composite formed a multiphase composite is shown in Figure 1. The double-inclusion fiber made of the piezoelectric shell and the core fiber is so called the active structural fiber (ASF). Long-cylindrical/ fibrous composite is concerned in the present work. The conventions presented in [29] is adopted. The fiber direction defined as the 3-direction. The ASF poling is taken in the transverse directions, the 1 and 2-directions. In the present case, for beam energy harvester model, the poling axis is in the thickness direction and defined by 1-direction as shown in Subsection 2.2, Figure 2.

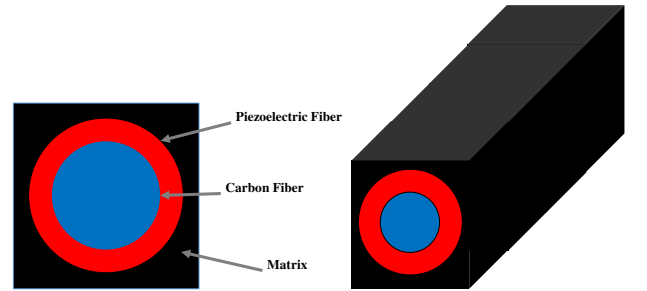


Figure 1: Multiphase Composite with Active Structural Fiber (ASF)

In the Double-Inclusion model, the effective electro-elastic matrix of the overall composite,  $\mathbf{E}_{iJMn}$ , as a function of each phase properties is shown in Equation (6). The electro-elastic matrices of each phase; the matrix, the piezoelectric shell, the

core fiber are defined by  $\mathbf{E}_{iJMn}^m$ ,  $\mathbf{E}_{iJMn}^p$  and  $\mathbf{E}_{iJMn}^c$ . In the following notations, superscripts  $m$ ,  $p$  and  $c$  denote the components of the matrix, the piezoelectric shell and the core fiber, respectively.

$$\mathbf{E}_{iJMn} = (V^m \mathbf{E}_{iJMn}^m \mathbf{A}^m) + (V^p \mathbf{E}_{iJMn}^p \mathbf{A}^p) + (V^c \mathbf{E}_{iJMn}^c \mathbf{A}^c) \quad (6)$$

The volume fractions of each phase to the overall composite volume are defined by  $V^m$ ,  $V^c$  and  $V^p$ . While  $\mathbf{A}^m$ ,  $\mathbf{A}^p$  and  $\mathbf{A}^c$  are the strain concentration tensors of each phase.

Lin and Sodano in [29] used the concentration tensors in the dilute limit to obtain the effective electro-elastic properties. In the present work, the Mori-Tanaka's method is applied to calculate the concentration tensors in order to obtain better agreement with experimental and computational results. The dilute and Mori-Tanaka's concentration tensors are calculated from

$$\begin{aligned} \mathbf{A}_{dil}^c &= (\mathbf{I} + (\mathbf{S}_{MnAb}^p \mathbf{E}_{iJMn}^m)^{-1} \mathbf{E}_{iJMn}^{cm})^{-1} \\ \mathbf{A}_{dil}^p &= (\mathbf{I} + (\mathbf{S}_{MnAb}^c \mathbf{E}_{iJMn}^m)^{-1} \mathbf{E}_{iJMn}^{cp})^{-1} \end{aligned} \quad (7)$$

$$\begin{aligned} \mathbf{A}_{MT}^m &= \mathbf{I} ((V^m \mathbf{I} + V^p \mathbf{A}_{dil}^p + V^c \mathbf{A}_{dil}^c)^{-1}) \\ \mathbf{A}_{MT}^p &= \mathbf{A}_{dil}^p ((V^m \mathbf{I} + V^p \mathbf{A}_{dil}^p + V^c \mathbf{A}_{dil}^c)^{-1}) \\ \mathbf{A}_{MT}^c &= \mathbf{A}_{dil}^c ((V^m \mathbf{I} + V^p \mathbf{A}_{dil}^p + V^c \mathbf{A}_{dil}^c)^{-1}) \end{aligned} \quad (8)$$

The dilute and Mori-Tanaka's concentration tensors are denoted by  $\mathbf{A}_{dil}$  and  $\mathbf{A}_{MT}$ , respectively. In Equation 6,  $\mathbf{A} = \mathbf{A}_{MT}$ .  $\mathbf{I}$  is a 9 x 9 identity matrix.  $\mathbf{E}_{iJMn}^{cm}$  and  $\mathbf{E}_{iJMn}^{cp}$  are obtained from  $\mathbf{E}_{iJMn}^c - \mathbf{E}_{iJMn}^m$  and  $\mathbf{E}_{iJMn}^p - \mathbf{E}_{iJMn}^m$ .

$\mathbf{S}_{MnAb}$  is the piezoelectric analog of the Eshelby's tensor. The detail derivation of the analytical form of this tensor is referred to [35]. In the present work, the numerical form of  $\mathbf{S}_{MnAb}$  [52] is used. Moreover, for a circular cylindrical fibrous case, if the ratio of the fiber length to its radius is very large ( $\rightarrow \infty$ ), a simplified form of  $\mathbf{S}_{MnAb}$  [41, 53] can be used.

## 2.2. Governing Piezoelectric Energy Harvester Voltage Equation

The piezoelectric energy harvester beam under dynamic bending excitation [25] is implemented for the energy harvesting evaluation in the present work. The governing voltage equation of the piezoelectric energy harvester is depicted in Equation (9).

$$\bar{U}(x) = \frac{i\omega\Gamma_2(x) \frac{\partial Z_{mech}(x)}{\partial x}}{-\frac{1}{R} + i\omega\Gamma_1(x) - i\omega\Gamma_2(x)^2 H_{\alpha m}(x)} \quad (9)$$

The voltage amplitude function exerted by the mechanical load is defined by  $\bar{U}(x)$ . The excitation frequency and the bending angle due to mechanical load are denoted by  $\omega$  and  $\partial Z_{mech}/\partial x$ . The  $H_{\alpha m}(x)$  represents the admittance function of the beam which relates the bending angle and the moment at the tip. In this formulation, the admittance function is derived as the reverse piezoelectric effect.  $R$  is the external resistance load. While  $i$  denotes the imaginary number,  $\sqrt{-1}$ . The material properties and the geometry are defined in  $\Gamma_1$  and  $\Gamma_2$  as follows

$$\Gamma_1 = \frac{bx}{h} \left( \varepsilon_{11}^T - \frac{d_{31}^2}{S_{33}} \right) \quad (10)$$

$$\Gamma_2 = \frac{d_{31}(h_u^2 - h_l^2)b}{2S_{33}h} \quad (11)$$

The geometry of the beam is shown in Figure 2. The active layer is the piezoelectric layer and the substrate layer made of non-piezoelectric material.  $b$  and  $h$  are the active layer width and thickness.  $x$  is the location along the beam length.  $h_u$  and  $h_l$  are the active layer upper and lower surfaces' heights to the neutral axis.

The conventions in Subsection 2.2 is followed, the 1-direction refer to the polling in the thickness direction and the 3-direction is in the longitudinal direction. In the present study, the active layer made of the multiphase composite is concerned. The layer is assumed made of uniformly distributed composite unit cells and periodically arranged in a square-packed or hexagonal array as shown by the illustration in Figure 3. Hence, the effective electro-elastic properties of Equation (6) is applicable as the effective electro-elastic properties of the active layer.

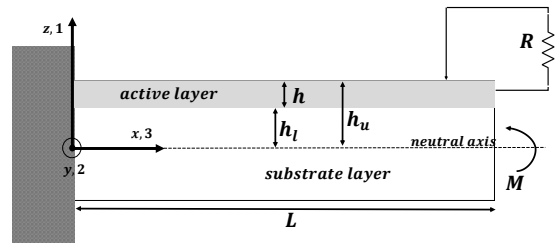


Figure 2: Piezoelectric Energy Harvester Beam

At the tip of the beam ( $x = L$ ), the voltage amplitude is calculated by

$$\bar{U}(L) = \frac{i\omega\Gamma_2(L) \frac{\partial Z_{mech}(L)}{\partial x}}{-\frac{1}{R} + i\omega\Gamma_1(L) - i\omega\Gamma_2(L)^2 H_{\alpha m}(L)} \quad (12)$$

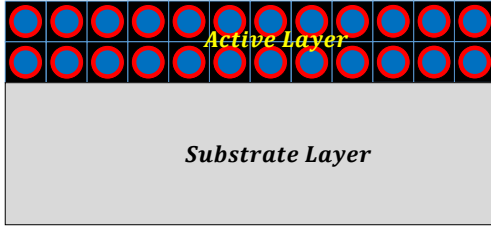


Figure 3: Cross-section of Energy Harvester Beam with Multiphase Composite Active Layer

From Equation (12), the maximum electrical power generated,  $P_{max}$  (Watt), could be expressed as

$$P_{max} = \frac{\bar{U}^2}{R} \quad (13)$$

### 2.3. Aircraft Weight Breakdown in Conceptual Aircraft Design

In the present work, the preliminary weight breakdown on aircraft design process [54] is adopted. The five main weight components of the aircraft are:

1. The empty weight,  $W_E$ , consisted of the aircraft structure and the installed equipment/interior.
2. The crew weight,  $W_C$ , and the payload weight,  $W_P$ . The payload consisted of the passenger included their baggage, and also the cargo. These weight components usually defined as the design requirements in the conceptual aircraft design.
3. The fuel weight,  $W_{fuel}$ , in which designed according to the aircraft mission profile, i.e., take-off, climb, cruise, descent, landing.
4. The take-off weight,  $W_{TO}$ , defined as the summation of all the above weight components as shown in Equation (14).

$$W_{TO} = W_E + W_C + W_P + W_{fuel} \quad (14)$$

In the conceptual aircraft design, the take-off weight initially calculated through an empirical formulation or the historical data. The empty weight ratio to the take-off weight can be determined from the empirical formulation in Equation (15).

$$\frac{W_E}{W_{TO}} = A W_{TO}^C K_{VS} \quad (15)$$

$A$  and  $C$  are varied based on the aircraft type. For a jet transport aircraft,  $A = 1.02$  and  $C = -0.06$ .  $K_{VS}$  is variable swept constant.  $K_{VS}$  equal to 1 for the

fixed swept wing and 1.04 for the variable swept wing. Thus, for jet transport aircraft with fixed swept, the empty weight fraction is

$$\frac{W_E}{W_{TO}} = 1.02 W_{TO}^{-0.06} \quad (16)$$

However, to be noted that the constant values in Equation (16) are derived based on the historical data of conventional jet transport aircraft. To the authors' knowledge, in the past decade, the commercial aircrafts just started to primarily utilize composites on their structure [55]. Therefore, there is still no adequate historical data to develop an empirical function for the empty weight fraction of jet transport aircraft with composites or advanced composites. Hence, for the study purpose in the present work, the weight fraction based on Equation (16) is also applied to the modified wingbox with multiphase composite. In a more detailed design process, some correction factors may be required to accommodate the structure with advanced composites. The interested reader is referred to the review in [56] for the prospective implementation of composite on future aircraft.

The weight iteration procedure may be required in the earliest design procedure. Initially, the  $W_E$ ,  $W_{fuel}$  and  $W_{TO}$  are unknown. Hence, the iterative process between Equation (14) and (15), as well as the fuel fraction through the mission profile, need to be conducted. However, in the present work, a reference aircraft is defined. The  $W_E$ ,  $W_{fuel}$  and  $W_{TO}$  of the reference aircraft are known. The changes of the weight components exerted by a material replacement are considered. Further detail of the weight evaluation process is explained in Subsection 3.3.

## 3. Algorithm and Procedure: Electro-elastic Properties Estimation, Energy Harvesting Analysis, Weight - Energy Evaluation

### 3.1. Effective Electro-elastic Properties Estimation of The Multiphase Composite

The procedure to calculate the piezoelectric Eshelby's tensor,  $\mathbf{S}_{MnAb}$ , is focused in this subsection. Once  $\mathbf{S}_{MnAb}$  tensor is known, the concentration tensor is evaluated via Equations (7) and (8). Then, the effective electro-elastic properties is obtained via Equation (6). The numerical form of  $\mathbf{S}_{MnAb}$  with Gauss integration procedure in [52] is adopted herein.

The elastic part of  $\mathbf{S}_{\mathbf{MnAb}}$  is given by

$$S_{MnAb} = \frac{E_{iJAb}}{8\pi} \sum_{p=1}^P \sum_{q=1}^Q (G_{MJin}^{pq} + G_{nJiM}^{pq}) W^p W^q$$

with  $M = 1, 2, 3$ ;

(17)

and the electro-elastic part is expressed as

$$S_{MnAb} = \frac{E_{iJAb}^m}{4\pi} \sum_{p=1}^P \sum_{q=1}^Q (G_{MJin}^{pq}) W^p W^q$$

with  $M = 4$

(18)

Where

$$G_{MJin}^{pq} = z_i^{pq} z_n^{pq} (K_{MJ}^{pq})^{-1}$$

$$K_{MJ}^{pq} = E_{iJm}^m z_i^{pq} z_n^{pq}$$

$i = 1, 2, 3; n = 1, 2, 3; J = 1, 2, 3, 4$

(19)

and

$$z_3^{pq} = \xi_3^p / a_3$$

$$z_1^{pq} = \sqrt{1 - (\xi_1^p)^2} \cos \theta^q / a_1$$

$$z_2^{pq} = \sqrt{1 - (\xi_2^p)^2} \cos \theta^q / a_2$$
(20)

The contracted Voigt's notation (i.e.,  $11 \rightarrow 1, 22 \rightarrow 2, 33 \rightarrow 3, 23 \rightarrow 4, 13 \rightarrow 5, 12 \rightarrow 6, 41 \rightarrow 7, 42 \rightarrow 8, 43 \rightarrow 9$ ) is used in Equations (17), (18) and (19). The four subscripts denoted the row and column in a  $9 \times 9$  matrix. Thus, for example  $S_{1111}$  represents the first row - first column component of the  $\mathbf{S}_{\mathbf{MnAb}}$  in a  $9 \times 9$  matrix form,  $S_{2243}$  is the second row - ninth column component, and so on.

The capital letters,  $P$  and  $Q$ , denote the number of the integration points. Where the superscripts  $p$  and  $q$  relate the parameter for each integration points,  $\xi_3^p$  and  $\theta^q$ , and the weight coefficients,  $W^p$  and  $W^q$ . The inclusion shape is generalised by the ellipsoidal shape with the semiaxes,  $a_1, a_2$  and  $a_3$  [35]. The semi-axis length of ellipsoid in longitudinal direction is defined by  $a_3$ . While  $a_1, a_2$  are the lengths in the transverse direction. Hence, for example, if the inclusion is a sphere particle then  $a_1 = a_2 = a_3$ , if the inclusion is a long cylindrical fiber then  $a_1 = a_2$  and  $a_3 \gg \gg a_1$ .

The procedure to evaluate the  $\mathbf{S}_{\mathbf{MnAb}}$  tensor is given as follow

1. The electro-elastic properties of the matrix material,  $\mathbf{E}_{\mathbf{iJMn}}^m$ , and the shape aspect ratio  $a_2/a_1$  and

$a_3/a_1$  as the input. As well as the number of integration points  $P$  and  $Q$  are determined. Then, the Gauss points,  $\xi_3^p$  and  $\theta^q$ , and the weight coefficients,  $W^p$  and  $W^q$  are obtained.

2.  $z_3^{pq}, z_1^{pq}$  and  $z_2^{pq}$  are calculated for each combination of the Gauss points via Equation (20).
3. The  $K_{MJ}^{pq}$  matrix component is evaluated for each combination of the Gauss points via Equation (19). The inverse of  $K_{MJ}^{pq}$  is used to determine  $G_{MJin}^{pq}$ .
4. The  $S_{MnAb}$  matrix component is evaluated via Equations (17) and (18).

A MATLAB<sup>®</sup> computational code is built to determine the  $\mathbf{S}_{\mathbf{MnAb}}$  matrix and as the effective electro-elastic properties,  $\mathbf{E}_{\mathbf{iJMn}}$ . The combination of various composite configuration is determined with the volume fraction of the ASF fiber to the overall composite,  $V_f$ , and the aspect ratio of the piezoelectric shell thickness to the ASF radius,  $AR$ . In the case of long-infinite fiber, the shape aspect ratio of the fiber is assumed very large,  $a_3/a_1 = 10^6$ . Moreover, the effective density,  $\rho$ , of the composite is also calculated in the present code by the linear summation of each phase density fraction.

### 3.2. Energy Harvesting Analysis via Hybrid Mathematical/Computational Procedure

In this subsection, the hybrid mathematical/computational model of the dynamic bending harvester model is presented. Figure 4 shows the flow of the voltage and power responses evaluation. The estimation of the structural deformation due to the actual mechanical load and the dummy load are two critical aspects of the energy harvesting analysis. The key outputs to be obtained from these load cases are:

1. The complex conjugate displacement slope or the bending angle exerted by the actual mechanical load,  $\partial Z_{mech}/\partial x$ . The actual load can be in the form of concentrated force, distributed pressure, moment, or even a relative motion case such as base excitation problem.
2. The admittance function,  $H_{\alpha m}$ , is defined as the bending angle a unit of moment. The dummy load is given as a unit of moment on the neutral axis of the beam tip. If the piezoelectric layers only cover a part of the beam length, the unit moment is given on the edge/tip of the piezoelectric layer, not on the tip of the beam.

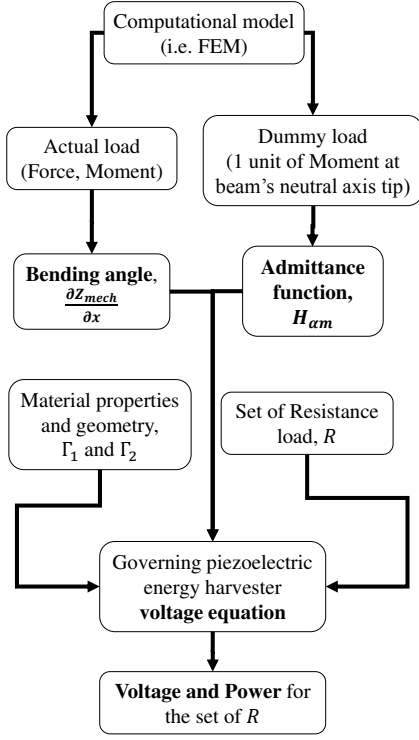


Figure 4: Schematic diagram of the energy harvesting analysis process

It is worth to remark that a full electro-mechanical coupling is not required in the hybrid mathematical/ computational scheme. The actual and dummy load simulations can be performed with standard structural analysis software. As explained in Subsection 2.2, the reverse piezoelectric effect is provided through the admittance function which obtained from the dummy load.

The next main process is the evaluation of the voltage and power responses based on Equations (9) and (13). The material properties and the geometry defined in  $\Gamma_1$  and  $\Gamma_2$  are used. A set of resistance load,  $R$ , is given as the external electrical load. A computational code is built using MATLAB<sup>®</sup> to evaluate the voltage and power responses.

### 3.3. Aircraft Weight - Energy Evaluation Procedure

In order to evaluate the aircraft weight and energy trade-off, firstly, the weight change due to material replacement is calculated. The empty weight,  $W_E$ , and the take-off weight,  $W_{TO}$  are directly affected by this change. Moreover, the fuel weight,  $W_{fuel}$ , is influenced and the new lift cruise load is applied for the dynamic response/energy harvesting analysis. The calculation process is depicted in Figure 5.

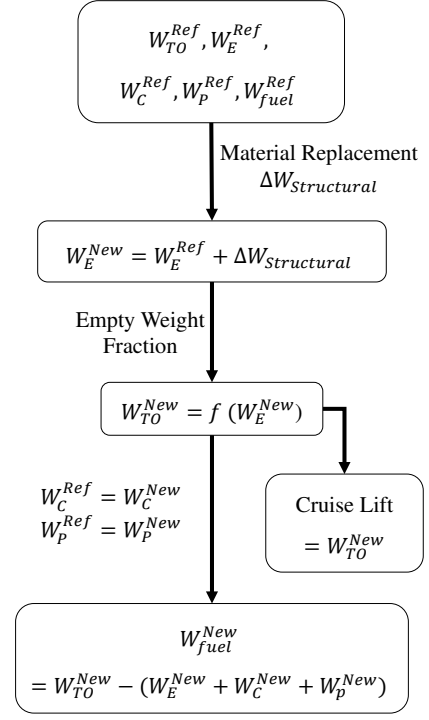


Figure 5: Schematic diagram of the weight change calculation

The description of the calculation process in Figure 5 is as follows:

1. Initially, the benchmark or original aircraft weight components are defined. In Figure 5, the original weight components denoted by the superscript "Ref".
2. The structural weight change,  $\Delta W_{Structural}$ , due to material replacement is concerned.
3. The new empty weight,  $W_E^{New}$ , is calculated as the original empty weight,  $W_E^{Ref}$ , with the weight change,  $\Delta W_{Structural}$ .
4. The empty fraction weight in Equation (15), or Equation (16) for jet transport aircraft is applied. The new take-off weight,  $W_{TO}^{New}$ , is obtained as a function of the new empty weight,  $W_E^{New}$ .
5. The new lift cruise load is equal to the  $W_{TO}^{New}$ .
6. The payload and crew weights are fixed, as these components are the aircraft design requirements and independent of the aircraft materials.
7. After the  $W_E^{New}$  and  $W_{TO}^{New}$  are calculated, the  $W_{fuel}^{New}$  is obtained via Equation (14).

In the present work, the aircraft structural change is caused by different wingbox upper skin material.

Two aircraft wings are concerned, the  $\Delta W_{Structural}$  is twice the weight change of a wingbox. The procedure to evaluate the weight and energy trade-off is developed. The electrical power harvested from the wingbox is compared with the APU generated power. The evaluation process of the fuel saving due to the structural change and the power harvested is shown in Figure 6.

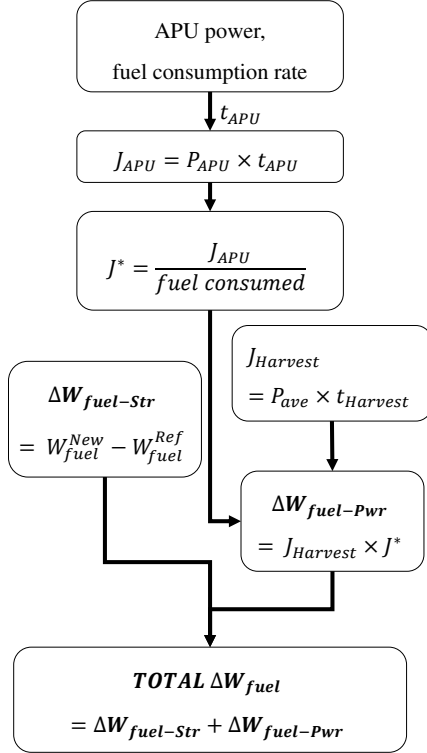


Figure 6: Schematic diagram of the fuel saving evaluation

The procedure in Figure 6 is described as follows:

1. The APU generated power (kW) and fuel consumption rate (kg/s or lbs/hour) are defined.
2. A certain operation time,  $t_{APU}$ , is concerned. The APU generated energy,  $J_{APU}$  (Joule), and the fuel consumed are calculated.
3. The ratio of the energy to the consumed fuel,  $J^*$  (Joule/kg-fuel or Joule/lbs-fuel), is obtained.
4. A harmonic oscillation in steady state is assumed. The average power harvested,  $P_{Ave}$ , is defined as half the maximum power  $P_{max}$ .
5. For a duration of vibration,  $t_{Harvest}$ , the energy generated by the harvester,  $J_{Harvest}$  (Joule), is calculated.
6. The equivalent fuel saved due to the energy harvested,  $\Delta W_{fuel-Pwr}$ , is calculated based on the  $J^*$  ratio.

7. The fuel change due to material replacement,  $\Delta W_{fuel-Str}$ , is defined as the variance between the new fuel weight the original fuel weight.
8. The TOTAL  $\Delta W_{fuel}$ , is the summation of the fuel change due to structure and the equivalent fuel saved from the energy harvested.

It is critical to remark, the formulation of maximum power in Equation (13) is derived for one cantilever beam. In the present work, the cantilever beam is associated with one aircraft wing. However, the total power harvested from the aircraft is considered for the equivalent fuel saved. Thus, the power harvested from the aircraft is twice the power harvested from a wing.

#### 4. Case Study and Validation: Multiphase Composite Electro-elastic Properties Estimation

The effective electro-elastic properties of various multiphase composite configurations obtained via the present Double-Inclusion code is discussed in this section. The results are compared against the analytical method, experimental work, and computational simulation. In addition, the dynamic analyses results of a lamina and a unimorph beam are shown in some details. The material properties are shown in Tables 1, 2 and 3.

Table 1: Material Properties of Piezoelectric Materials

Property	PZT-7A [42]	PZT-5A [57]	BaTiO <sub>3</sub> [58]
$C_{11}$ (GPa)	148.0	120.3	150.4
$C_{12}$ (GPa)	76.2	75.2	65.6
$C_{13}$ (GPa)	74.2	75.1	65.9
$C_{33}$ (GPa)	131	110.9	145.5
$C_{44}$ (GPa)	25.4	21.0	43.9
$C_{66}$ (GPa)	35.9	22.7	42.4
$e_{31}$ (N/Vm)	-2.1	-5.2	-4.3
$e_{33}$ (N/Vm)	9.5	15.9	17.3
$e_{15}$ (N/Vm)	9.2	12.3	11.4
$\epsilon_{11}^S/\epsilon_0$	460	919.1	1115.1
$\epsilon_{33}^S/\epsilon_0$	235	826.6	1251.3
$\rho$ (kg/m <sup>3</sup> )	7600	7750	5700

##### 4.1. Electro-elastic Properties Comparison against Analytical Model and Experimental Results

In the following case, the results of the present Double-Inclusion code is compared against the ana-

Table 2: Material Properties of Core Fiber Materials

Property	Carbon	SiC	Glass
	Fiber [42]	Fiber [42]	Fiber [59]
$C_{11}$ (GPa)	24.0	483.7	88.8
$C_{12}$ (GPa)	9.7	99.1	29.6
$C_{13}$ (GPa)	6.7	99.1	29.6
$C_{33}$ (GPa)	243.7	483.7	88.8
$C_{44}$ (GPa)	27.0	192.3	29.6
$C_{66}$ (GPa)	11.0	192.3	29.6
$e_{31}$ (N/Vm)	0	0	0
$e_{33}$ (N/Vm)	0	0	0
$e_{15}$ (N/Vm)	0	0	0
$\varepsilon_{11}^S/\varepsilon_0$	12.0	10.0	6.4
$\varepsilon_{33}^S/\varepsilon_0$	12.0	10.0	6.4
$\rho$ (kg/m <sup>3</sup> )	2000	4360	2550

Table 3: Material Properties of Matrix Materials

Property	LaRC-SI	Epoxy
	[42]	[59]
$C_{11}$ (GPa)	8.1	8.0
$C_{12}$ (GPa)	5.4	4.4
$C_{13}$ (GPa)	5.4	4.4
$C_{33}$ (GPa)	8.1	8.0
$C_{44}$ (GPa)	1.4	1.4
$C_{66}$ (GPa)	1.4	1.4
$e_{31}$ (N/Vm)	0	0
$e_{33}$ (N/Vm)	0	0
$e_{15}$ (N/Vm)	0	0
$\varepsilon_{11}^S/\varepsilon_0$	2.8	4.2
$\varepsilon_{33}^S/\varepsilon_0$	2.8	4.2
$\rho$ (kg/m <sup>3</sup> )	1360	1150

lytical model and experimental results of single fiber composite by Chan and Unsworth [40]. A combination of PZT-7A, Carbon Fiber and Epoxy Matrix from Tables 1, 2 and 3 is used as the composite materials. It is important to notice that Chan and Unsworth found  $d_{33}$  of the tested PZT-7A is around 163-167 pm/V, hence 167 pm/V is used in their mathematical model [40]. In the present work,  $e_{33}$  is changed to 12.3 C/m<sup>2</sup>, thus  $d_{33}$  is 167 pm/V and  $d_{31}, d_{32}$  are kept as -60 pm/V.

The variation of stiffness, compliance and piezoelectric coupling parameters of the multiphase composite with the ASF volume fraction and piezoelectric aspect ratio are shown in Figure 7. The "Present Code - DI MT" denotes the results obtained by means of the present Double-Inclusion code. "AR1", "AR2",

"AR3" and "AR4" presented the values for 0.50, 0.60, 0.70 and 0.95 piezoelectric shell aspect ratios. Meanwhile, the results of Chan-Unsworth single fiber model are depicted by the solid black line.

It is clearly seen in Figure 7, the results obtained by the present code show the similar trend as predicted by Chan-Unsworth model. As the aspect ratio of the piezoelectric shell increases, the pattern of the multiphase composite shifted closer to the results of single fiber model. It can be seen at 0.95 piezoelectric aspect ratio, the results of multiphase composite and single fiber model coincide. In this case, the ASF is 99.75% consisted of piezoelectric material. Hence, the multiphase composite behaves almost like a single piezoelectric fiber composite.

The stiffness component of the composite in the fiber direction is shown in Figure 7a. As the carbon fiber and PZT-7A stiffness components are larger than the epoxy matrix, the composite stiffness increases with the ASF volume fraction for a particular aspect ratio. In contrast, as the carbon fiber stiffness is larger than PZT-7A, the composite stiffness decreases while the aspect ratio increases.

In Figure 7b, the piezoelectric constant of stress-charge form,  $e_{33}$ , is depicted. As the aspect ratio increases, the PZT-7A composition is larger. Thus, the piezoelectric constant of the composite is increased. As well as for a particular aspect ratio,  $e_{33}$  is increased with the volume fraction.

The components in strain-charge form, compliance,  $S_{31}$ , and piezoelectric charge constant,  $d_{31}$ , are presented in Figures 7c and 7d. To not be confused that the negative (-) sign represents the cause and effect in opposite direction. For example, more negative value of  $d_{31}$ , means larger deformation in negative direction (compression) due to a particular positive voltage.

Interesting to note that for both  $S_{31}$  and  $d_{31}$ , the trend of the parameters for large volume fraction (above 50%) are insignificantly changed as the volume fraction increased. In particular, for  $d_{31}$ , shows that at large volume fraction, a further increment of the volume fraction will not significantly change the electrical response of the composite due to a structural deformation.

The variation of the other compliance and piezoelectric charge constant components, as well as the dielectric permittivity and density of the multiphase composite, are depicted in Figure 8. In Figure 8, the comparison against the experimental results of Chan-Unsworth [40] is also shown.

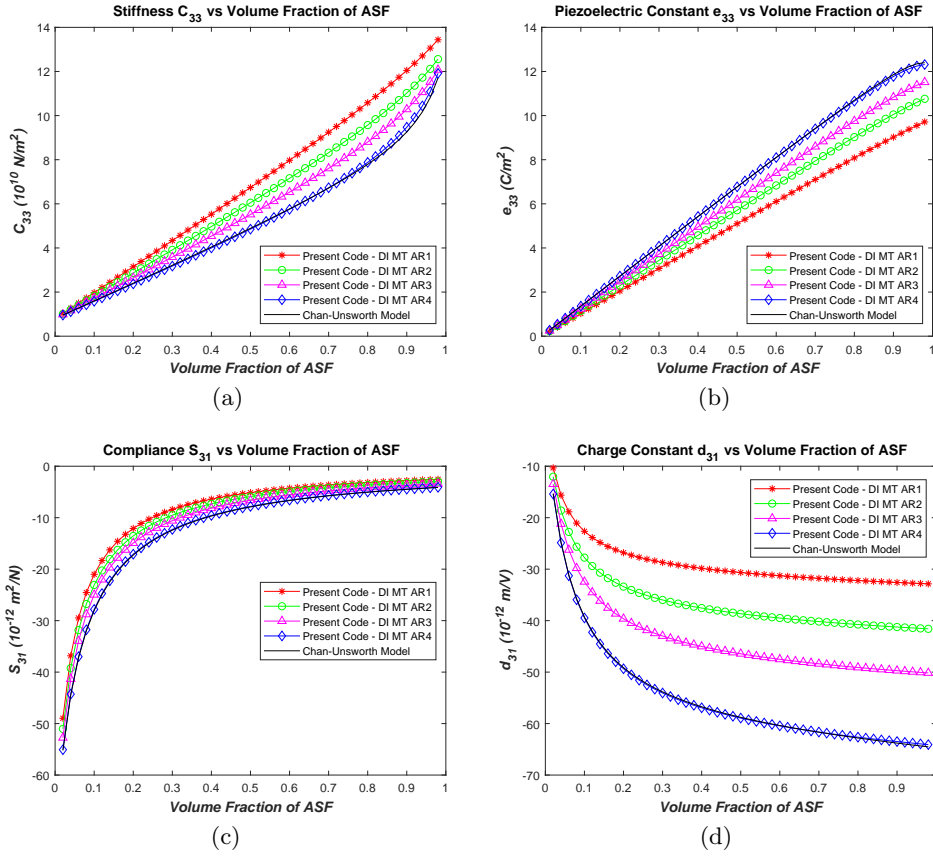


Figure 7: (a) Stiffness,  $C_{33}$ , (b) Piezoelectric Constant,  $e_{33}$ , (c) Compliance,  $S_{31}$ , and (d) Charge Constant,  $d_{31}$ , vs ASF Volume Fraction of PZT-7A-Carbon Fiber-Epoxy Composites

It can be seen that all the parameters in Figure 8 show the same trend as both the mathematical model and experimental results of Chan-Unsworth. As displayed in Figures 8a and 8b, both the density,  $\rho$ , and the charge constant,  $d_{33}$ , of the multiphase composite at 0.95 aspect ratio are coincide with the Chan-Unsworth model and in a close agreement with the experimental results. As the densities of the ASF materials are larger than the epoxy matrix, the density of the composite increases linearly with the volume fraction at the same aspect ratio. Meanwhile, similar with the  $d_{31}$  trend shown in Figure 7d, the charge constant,  $d_{33}$ , above 50% volume fraction almost insensitive to the volume fraction increment.

Mathematically, by stiffness matrices inverse, it is found the compliance of carbon fiber at 11-direction is more positive than PZT-7A, while the carbon fiber's compliance at 12-direction is more negative. Hence, the compliance components,  $S_{11}$  and  $S_{12}$  of the ASF decrease and increase together with the increasing aspect ratio. Figure 8c shows the aspect ratio variation is insignificant to the summation of  $S_{11}$  and  $S_{12}$ .

Despite the fact that most of the parameters in Figures 7 and 8 show good comparisons between the present model and Chan-Unsworth model/experiment's results, some discrepancies can be seen as depicted in Figure 8c. Chan and Unsworth in [40] stated that the differences between the model and the experimental results occurred due to the variations of the tested materials properties and the manufacturer data. As previously explained, the charge constant,  $d_{33}$ , for the present and Chan-Unsworth models is adjusted the same as the experimental value. However, the other properties are kept the same with manufacturer data as their deviations from tested samples are not available in [40].

In addition, the differences between both models may occur due to the models are derived from different approaches. The Chan-Unsworth model is derived based on the rule of mixture, in which the effective properties are a function of the volume fraction and fiber/matrix properties. While the present model utilizes the Eshelby's tensor with Mori-Tanaka method where the inclusion's shape is also considered.



the aspect ratio increases, the charge constant ratio shifted towards the single fiber model. Moreover, similar with Figure 7d the charge constant ratio also less sensitive to the volume fraction increment at above 50% volume fraction. Moreover, at a small aspect ratio, 0.21, the charge constant ratio is almost constant.

In detail, the variances of the present model and Lin-Sodano's model in [32] against the experimental results are shown in Table 4. The maximum variances of both models occur at aspect ratio 0.21 with variances more than 20%. These variances arise due to some jumps in the experimental values, i.e., at the aspect ratio 0.21 and volume fraction 23.6%.

Table 4: Table of Variances: The Present Model and Lin-Sodano Model [32] against The Experimental Results

	Table of Variances, $\Delta$			
	AR	Min. $\Delta$	Max. $\Delta$	Average $\Delta$
Lin -	0.21	0.01 %	21.9 %	9.8 %
Sodano	0.42	1.34 %	9.13 %	5.4 %
Model [32]	0.60	4.62 %	13.0 %	9.2 %
Present	0.21	0.01 %	29.17 %	14.47 %
Code	0.42	0.01 %	11.18 %	4.81 %
DI-MT	0.60	0.04 %	4.54 %	2.40 %

#### 4.2. Electro-elastic Properties Comparison against Finite Element Model

In this subsection, static and dynamic analyses of the multiphase composite performed via finite element method (FEM) is discussed. The comparison between the present Double-Inclusion code and the FEM results is presented. The single lamina composites in the form of long cube/unit cell, similar as shown in Figure 1, are used in the FEM simulation. On the static analysis, FEM results of Lin-Sodano [29] and XFEM results of Koutsawa et al. [60] are used as the benchmarks. The modal analysis of the single lamina composite is performed as part of the dynamic analysis. In addition, the dynamic response of a unimorph beam is also investigated. The results of the modal and dynamic response analysis are shown in some details.

##### 4.2.1. Static analysis of single lamina composite

In Figure 10, the modulus and relative permittivity at the longitudinal and transversal directions of the multiphase composites consisted of PZT-7A - Carbon fiber - LaRC SI matrix is depicted. The present code results are denoted by the solid line with the symbols,

while the Lin-Sodano FEM results are shown by the symbols only. "AR1", "AR2", "AR3" and "AR4" denoted by the star, circle, triangle, and diamond symbols which represent 0.2, 0.4, 0.6 and 0.8 aspect ratios.

Various electrical and mechanical boundary conditions were applied to the single lamina FEM model in [29] to investigate the electro-elastic properties of the composite. Static load condition was implemented. Eight variations of electro-mechanical boundary conditions were used to obtain four stiffness components, two permittivity components, and two piezoelectric coupling components. Thus, for one combination of aspect ratio and volume fraction, at least eight static FEM simulations are required. The electro-mechanical boundary conditions are explained in more details in [29, 42].

It can be seen in Figures 10a and 10b, the properties at longitudinal/fiber direction,  $E_3$  and  $\varepsilon_{33}^S/\varepsilon_0$ , the present code and FEM results are essentially the same trends. Insignificant discrepancies between the two results are seen. The Young's modulus,  $E_3$ , for all aspect ratios increase linearly with the volume fraction, as the composite becomes stiffer with larger piezoelectric and carbon fiber fraction. However, the  $E_3$  decreases as the aspect ratio increases. In this case, the stiffness is lesser with a smaller fraction of carbon fiber. In contrast, the relative permittivity,  $\varepsilon_{33}^S/\varepsilon_0$ , increases with the volume fraction and aspect ratio. The piezoelectric possesses the largest permittivity amongst the other components. Thus, larger piezoelectric fraction provides more permittivity.

The properties at the transversal direction,  $E_1$  and  $\varepsilon_{11}^S/\varepsilon_0$  are depicted in Figures 10c and 10d. To be noted here, due to orthotropic condition, the properties at 1-direction and 2-direction are equal. Different with the properties at the longitudinal direction, the properties at transversal direction grow exponentially with the volume fraction. The stiffness components of the piezoelectric at the transversal direction are in a larger order than the carbon fiber; hundreds GPa compare to tens GPA. Thus, at large piezoelectric fraction, the piezoelectric stiffness dominates the effective stiffness of the composite. A similar condition is also observed in the permittivity component, as the permittivity components of the piezoelectric at the transversal direction are in a much larger order than the carbon fiber and matrix.

However, it is noted for the properties at the transversal direction; discrepancies occur between the

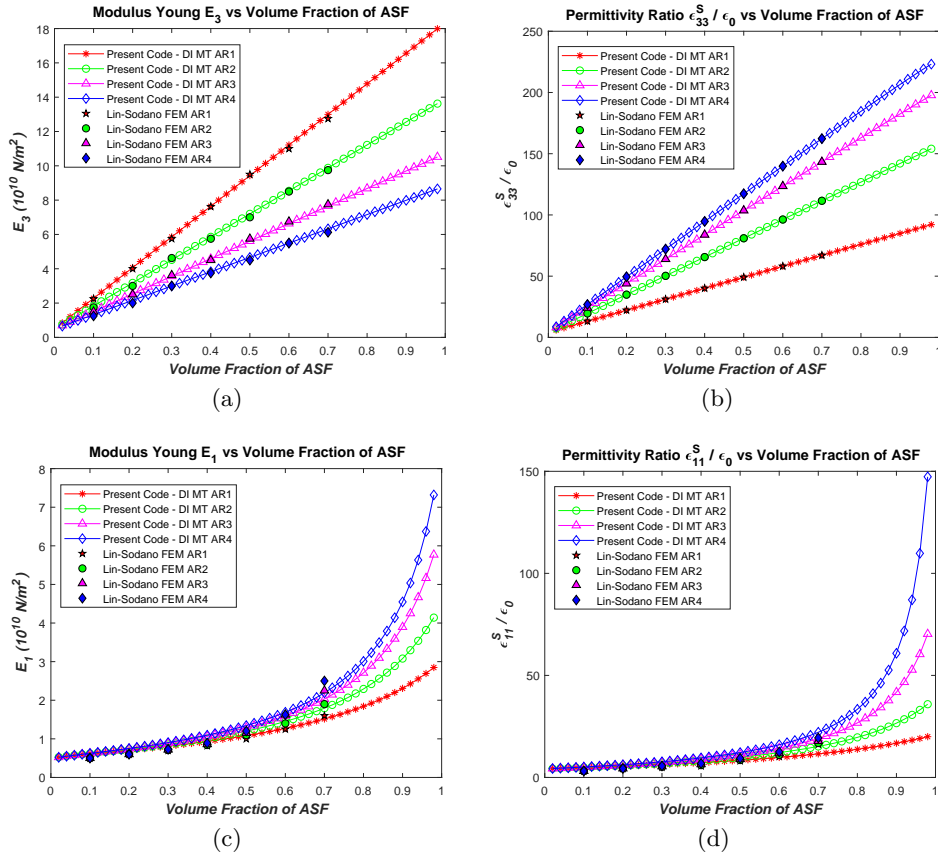


Figure 10: (a) Modulus Young,  $E_3$ , (b) Relative Permittivity,  $\varepsilon_{33}^S/\varepsilon_0$ , (c) Modulus Young,  $E_1$ , and (d) Relative Permittivity,  $\varepsilon_{11}^S/\varepsilon_0$ , vs ASF Volume Fraction of PZT-7A - Carbon Fiber - LaRC-SI Composites

present code and the FEM results. At the large volume fraction ( $>50\%$ ), the FEM resulted in larger increment rate of  $E_1$ . The FEM estimated an almost similar rate of increment for the relative permittivity,  $\varepsilon_{11}^S/\varepsilon_0$ , to the volume fraction at all aspect ratios. Thus, with small aspect ratio, the increment rate is higher than the present code, while at large aspect ratio the increment rate is lower than the present code.

These results aligned with the phenomena observed in [29]. The maximum discrepancies occurred at 70% volume fraction between the model and the FEM results in [29]. At 70% volume fraction, the model overestimated the  $E_1$  by 31% and 39% at 0.8 aspect ratio. While at 70% volume fraction and 0.2 aspect ratio, it overestimates the  $\varepsilon_{11}^S/\varepsilon_0$  by 39%. Despite the fact that the maximum differences also occur at the same ASF compositions for the present code, a better agreement with the FEM results is obtained. At 70% volume fraction and 0.8 aspect ratio, the present code possesses 12% variance of  $E_1$ . While at 0.2 aspect ratio, it overestimates the  $\varepsilon_{11}^S/\varepsilon_0$  by 28%.

The comparison of the present code and the XFEM

results of Koutsawa et al. [60] is shown in Figure 11. The glass fiber is used as the core fiber, and the epoxy is used as matrix. By means of XFEM, Koutsawa et al. applied enrichment functions and level set method to model different material properties at the specific region of the multiphase composite. Thus, the meshing of the finite element is independent of the phase of the composite [60].

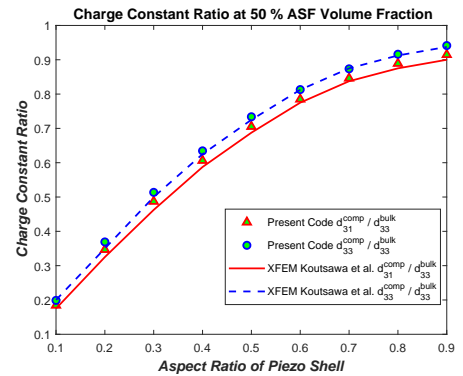


Figure 11: Charge Constant Ratio  $d_{31}^{comp}/d_{31}^{bulk}$  &  $d_{33}^{comp}/d_{33}^{bulk}$ , vs Aspect Ratio of PZT-7A - Glass - Epoxy Composites

Figure 11 shows an excellent agreement between the present code and XFEM results. Both the charge constant ratio for 33-directions and 31-directions are in similar trends. Initially, with small aspect ratio, the charge constant ratio increases almost linearly with the aspect ratio. The increment rate, however, decreases at a larger aspect ratio (>40%). These results support the trends previously shown in Figures 7d, 8b and 9, in which the charge constants increase with the aspect ratio. In more detail, the comparison of  $d_{31}$  ratios obtained from the present model and XFEM can be seen in Table 5.

Table 5: Charge Constant Ratio Comparison: The Present Model vs XFEM - Koutsawa et al. [60]

AR	Charge Constant Ratio ( $d_{31}^{comp}/d_{31}^{bulk}$ )		
	Present Code	XFEM [60]	$\Delta$ (%)
0.1	0.19	0.18	5.56%
0.2	0.35	0.33	6.06%
0.3	0.49	0.46	6.52%
0.4	0.61	0.59	3.39%
0.5	0.71	0.69	2.90%
0.6	0.79	0.78	1.28%
0.7	0.85	0.84	1.19%
0.8	0.89	0.88	1.14%
0.9	0.91	0.90	1.11%

#### 4.2.2. Dynamic analysis of single lamina composite and unimorph beam

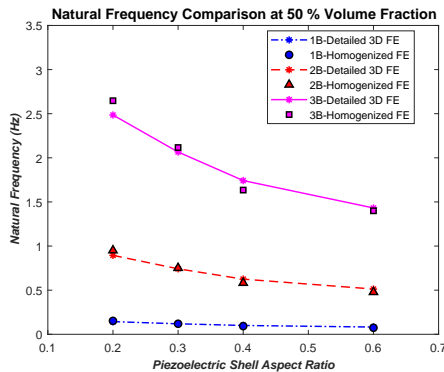


Figure 12: Natural Frequency Comparison for Different Aspect Ratio at 50% Volume Fraction of PZT-5A - Carbon - LaRC-SI Composites

In this section, modal analysis of a single lamina of the multiphase composite is concerned. Two types of model are used in the FEM simulation to compare the displacement and voltage distribution of the lamina. The first model is a long cube/unit-cell with detailed

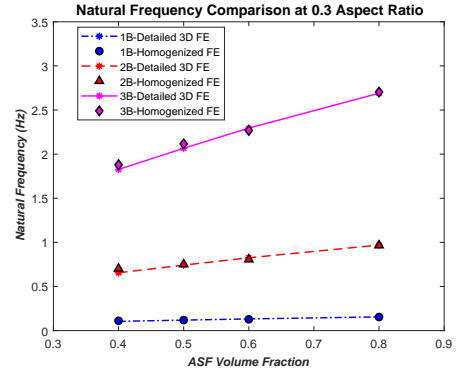


Figure 13: Natural Frequency Comparison for Different Volume Fraction at 0.3 Aspect Ratio of PZT-5A - Carbon - LaRC-SI Composites

3D FEM of each phase, i.e., the core fiber, piezoelectric shell, matrix and their respective material properties. This model is similar as shown in Figure 1. The second model is a simple long cube without the detail of each phase and the effective electro-elastic properties applied. Herein and hereafter, The first and the second model are denoted by "Detailed 3D FE" and "Homogenized FE", respectively.

The FEM simulation is performed using COMSOL Multiphysics<sup>®</sup>. The piezoelectric devices module is applied. Due to the limitation of the software, only linear tetrahedral elements are used. The model is fixed at one end. The observed multiphase composites consisted of PZT-5A, Carbon fiber, and LaRC-SI matrix. The bending natural frequencies comparison of the "Detailed 3D FE" and "Homogenized FE" models are shown in Figures 12 and 13.

Figure 12 depicted the natural frequencies of the multiphase composites for 50% ASF volume fraction. The first, second and third bending modes are denoted by "1B", "2B" and "3B". It can be seen, the natural frequency of the composite decreases as the aspect ratio increases. This behaviour supports the trend previously shown in Figures 10a and 8a. For a particular volume fraction, the composite is less stiff and heavier as the aspect ratio increases. Both the "Detailed 3D FE" and "Homogenized FE" models are in a close agreement.

Figure 13 displayed the natural frequencies of the multiphase composites for 0.3 piezoelectric shell aspect ratio. As shown previously in Figure 10a, the composite becomes stiffer as the volume fraction increases. Although the density also increases with the volume fraction, the increment rate is lower than the Young's modulus increment rate. Thus, the natu-

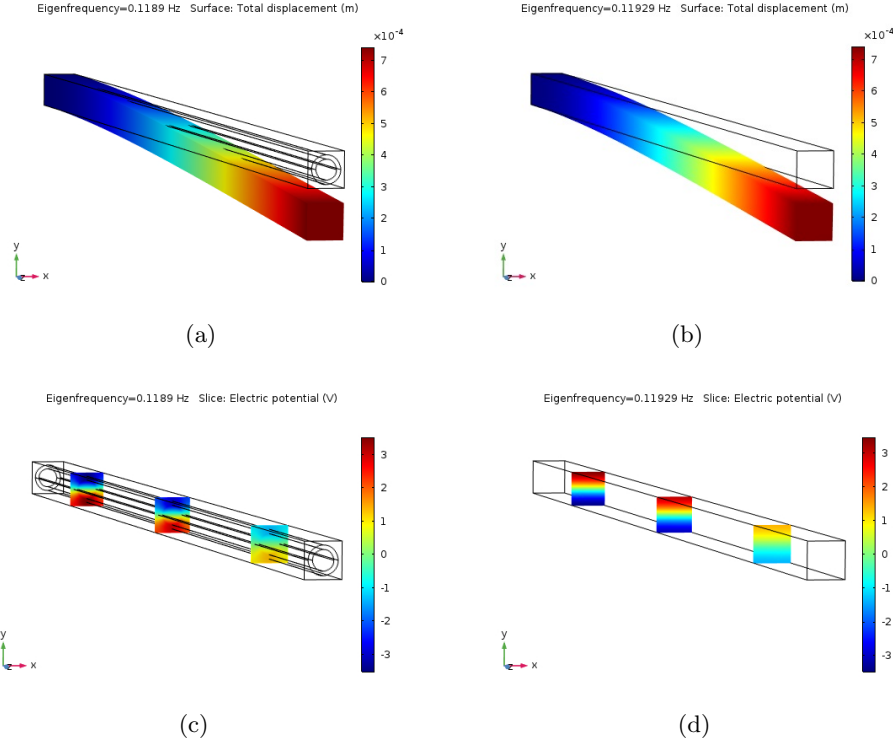


Figure 14: (a) Detailed 3D FE Displacement Eigenvector (b) Homogenization FE Displacement Eigenvector (c) Detailed 3D FE Voltage Eigenvector and (d) Homogenization FE Voltage Eigenvector of The 1st Bending Mode, PZT-5A - Carbon Fiber - LaRC-SI Composites with 50% Volume Fraction and 0.3 Aspect Ratio

Table 6: Natural Frequency Comparison for Different Volume Fraction at 0.3 Aspect Ratio of PZT-5A - Carbon - LaRC-SI Composites, Detailed 3D Finite Element vs Finite Element with Homogenization Properties

Vf	Mode	Natural frequency (Hz)		
		Detailed 3D	Homogenized	$\Delta$ (%)
50%	1B	0.1189	0.1192	0.31%
	2B	0.7423	0.7513	1.32%
	3B	2.0662	2.1166	2.44%
60%	1B	0.1323	0.1281	3.14%
	2B	0.8254	0.8062	2.32%
	3B	2.2950	2.2684	1.16%
80%	1B	0.1556	0.1540	1.02%
	2B	0.9695	0.9657	0.40%
	3B	2.6902	2.7037	0.50%

ral frequency increases with the volume fraction as displayed in Figure 13. More details of the natural frequency comparison for different volume fraction is shown in Table 6. The variances between both models are insignificant ( $<5\%$ ).

Concerning the energy harvesting formulation, the natural frequencies with and without activated piezo-

electric effect are compared. The algorithm for the hybrid mathematical/computational as shown in Figure 4 is purposed in particular to evaluate the energy harvested utilizing a standard computational method, i.e., FEM, without electro-mechanical coupling. Thus, it is considered important to compare the differences between models with and without electromechanical coupling. Table 7 depicted the comparison of both models for the "Homogenized FE".

Table 7 displayed the natural frequencies for different aspect ratio at 50% volume fraction. "Elec-Mech" denotes the model with activated electro-mechanical coupling. The model without electro-mechanical coupling, pure mechanical response, is denoted by "Pure Mech". The natural frequencies of both models are in good comparison. In particular, the variances for 1st bending modes are almost negligible. Therefore, it can be assumed the bending natural frequency is almost not affected with/without electro-mechanical coupling for the current multiphase configuration.

The example of the 1st bending displacement and voltage mode shape for both "Detailed 3D FE" and "Homogenized FE" models are shown in Figure 14. The models shown consisted of 50% ASF with 0.3

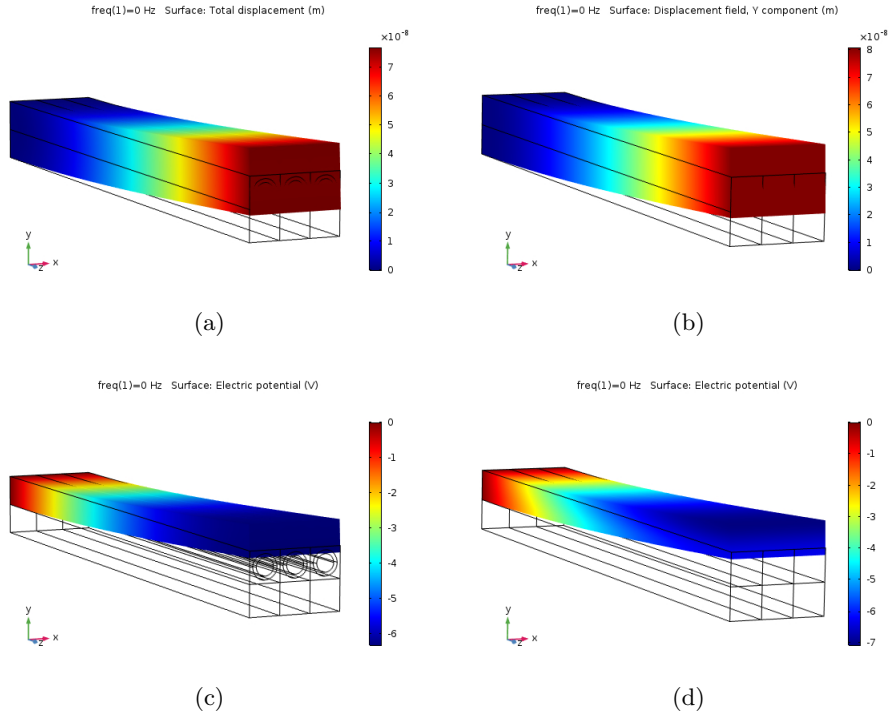


Figure 15: (a) Detailed 3D FE Displacement (b) Homogenization FE Displacement (c) Detailed 3D FE Voltage and (d) Homogenization FE Voltage of The Static Bending Response, PZT-5A - Carbon Fiber - LaRC-SI Unimorph Beam with 50% Volume Fraction - 0.3 Aspect Ratio and Aluminium Substrate

Table 7: Natural Frequency Comparison of Homogenized FE for Different Volume Fraction at 50% Volume Fraction of PZT-5A - Carbon - LaRC-SI Composites, Pure Mechanical Effect vs Activated Electro-mechanical Coupling

AR	Mode	Natural frequency (Hz)		
		Elec-Mech	Pure Mech	$\Delta$ (%)
0.2	1B	0.1521	0.1519	0.13%
	2B	0.9508	0.9452	0.59%
	3B	2.6470	2.6174	1.12%
0.3	1B	0.1192	0.1195	0.25%
	2B	0.7513	0.7468	0.60%
	3B	2.1166	2.0809	1.69%
0.4	1B	0.0926	0.0927	0.11%
	2B	0.5819	0.5780	0.67%
	3B	1.6345	1.6219	0.77%

aspect ratio. At this composition, the ASF is half of the composite, and the core fiber is half of the ASF. Both displacement and voltage contours are in good comparison. The displacement contours in Figures 14a and 14b both depicted maximum displacements at the tip.

The sliced contours of the voltage shown in Figures 14c and 14d. It can be seen that the voltage is max-

imum near the root and decreases towards the tip. In the cross-sectional slice, it can be seen that the voltage of the top and bottom part are the opposite values. The top part exhibits tension and the bottom part exhibits compression. Meanwhile, the voltage at the neutral axis is zero.

The modal and dynamic response analyses of a unimorph beam are also performed using FEM. The unimorph beam commonly consisted of two layers, substrate, and active layers. A non-piezoelectric material is used as the substrate and piezoelectric material as the active layer. In the present work, the bulk piezoelectric material is replaced by the multiphase composite as the active layer.

Table 8: Natural Frequency Comparison for The Unimorph Beam, Detailed 3D Finite Element vs Finite Element with Homogenization Properties

Mode	Natural frequency (Hz)		
	Detailed 3D	Homogenized	$\Delta$ (%)
1B	1.5618	1.4347	8.13%
2B	7.8235	7.8421	0.24%
1T	8.5433	8.3114	2.71%

In the present case, the active layer consisted of

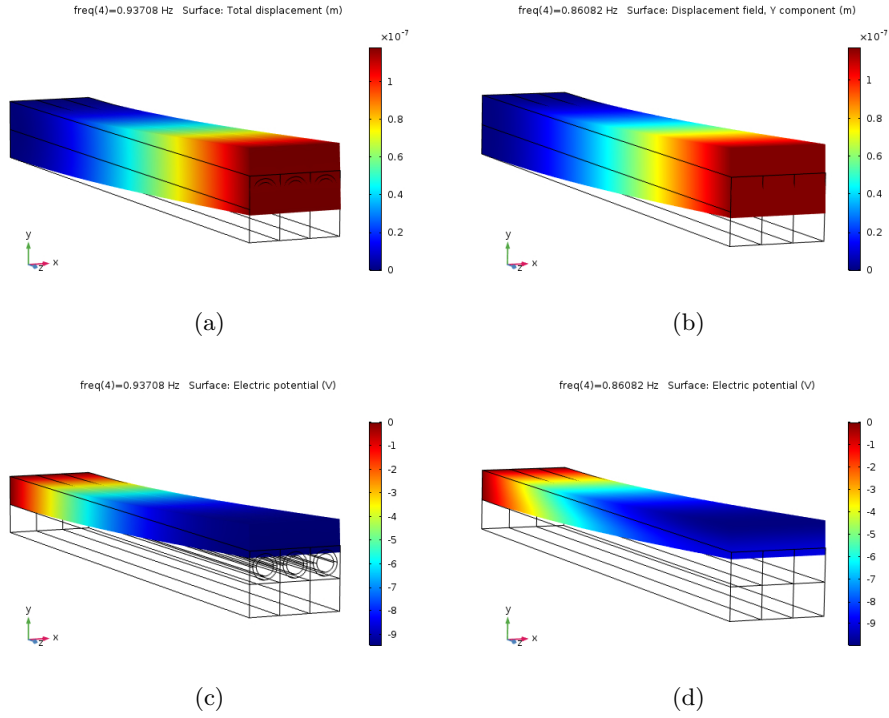


Figure 16: (a) Detailed 3D FE Displacement (b) Homogenization FE Displacement (c) Detailed 3D FE Voltage and (d) Homogenization FE Voltage of The Dynamic Bending Response at 0.6 Frequency Ratio, PZT-5A - Carbon Fiber - LaRC-SI Unimorph Beam with 50% Volume Fraction - 0.3 Aspect Ratio and Aluminium Substrate

three multiphase composite laminae arranged in a row. The multiphase composite with 50% volume fraction and 0.3 aspect ratio is used. An aluminum layer is used as the substrate at the bottom. The natural frequencies comparison of the unimorph with "Detailed 3D FE" and "Homogenized FE" is shown in Table 8. The first bending, second bending and the first torsion modes are denoted by "1B", "2B" and "1T". The variances of both models are on a reasonable scale.

In the dynamic response analysis, a sensor-like problem is investigated. The unimorph's displacement and voltage responses exerted by an external mechanical load at the tip. The responses at static condition, 0 Hz excitation frequency, is shown in Figure 15. It can be seen that the deformation of the unimorph with "Detailed 3D FE" is slightly lower than the "Homogenized FE". The "Detailed 3D FE" unimorph is slightly stiffer than the "Homogenized FE" due to the use of the tetrahedral element. This element is known to have a stiff characteristic in bending load case. Although coarse meshes are used for both models, the "Detailed 3D FE" converged at a much higher number of elements due to its complex geometry.

A frequency ratio is defined here as the ratio of the excitation frequency to the 1st bending natural frequency. Figure 16 depicted the unimorph responses for 0.6 frequency ratio excitation. In this case, 0.6 frequency ratio for the "Detailed 3D FE" equals with  $0.6 \times 1.5618$  Hz or 0.9371 Hz. As the excitation frequency increases near the natural frequency, the resonance occurs, and the deformation amplitude is largely magnified. Thus, it is considered reasonable to compare the responses below the natural frequency, hence frequency ratio is used. It is obviously seen that the displacement and voltage amplitudes of both "Detailed 3D FE" and "Homogenized FE" models are in a good comparison.

## 5. Wingbox Energy Harvesting Simulation

The energy harvesting simulation for a notional civil jet aircraft wingbox is performed in the present work. The structural dynamic response of the aircraft due to cruise load excitation is investigated. The excitation frequencies lower than the 1st bending mode natural frequency is observed. The wingbox model is analyzed by applying the frequency-dependant forced excitation via a FEM module.

The aircraft wingbox model used in the present work is based on the model used in [25]. The dimensions of the model are 14.48 m half span, 2.29 m root chord and 0.88 m tip chord. This model is a simplification of a typical civil jet aircraft wingbox for a long-range flight in [61]. The details of the simplification process are referred to [25]. The wingbox layout from topside view is shown in Figure 17.

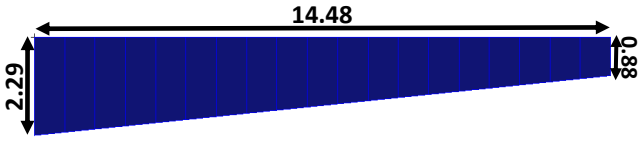


Figure 17: Wingbox topside view (unit in meters)

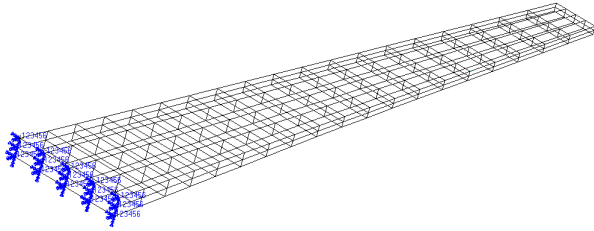


Figure 18: Wingbox model for finite element analysis

All of the wingbox components are originally made of Aluminium Alloy, Al-2219, with Young's modulus 73.1 GPa and density 2840 kg/m<sup>3</sup>. For energy harvesting purpose, the upper skin material is replaced by a piezoceramic material, M1832 [62], with longitudinal Young's modulus 70.7 GPa and density 8100 kg/m<sup>3</sup> in [25].

In the present case, due to the unavailability of complete material properties in 3D form, M1832 is replaced by a more common piezoelectric material, PZT-5A. The PZT-5A is also selected due to its high piezoelectric coupling parameters. Furthermore, The PZT-5A is combined with carbon fiber and LaRC-SI to form the multiphase composite. The multiphase

composites fiber is oriented along the span from the root to the tip. The wingbox weight with different bulk piezoelectric materials is shown in Table 9. Furthermore, the wingbox weight with various composition of multiphase composite as the upper skin is shown in Tables 10 and 11.

Figure 18 shows the wingbox model used for the FEM simulation. The skins, ribs, and spars are modeled as quadrilateral shell elements. In this case, the material properties of the piezoelectric/ multiphase composite in 3D form is reduced to 2D form. The procedure to reduce the material properties is referred to [57]. The translation and the rotation degree of freedoms are fixed at the root. The load for one wingbox is equal with half of the aircraft lift during cruise flight. In this case, the aerodynamic lift load assumed equal to the take-off weight,  $W_{TO}$ . Hence, the lift load is dependent on the upper skin material used.

Table 9: Wingbox Weight: Different Upper Skin Material

Material	Al-2219 [25]	M1832 [25]	PZT-5A
Weight (lbs)	2415	4100	3929

Table 10: Wingbox Weight: Multiphase Composites Upper Skin, PZT-5A - Carbon - LaRC-SI 50% Volume Fraction

Aspect Ratio	0.2	0.4	0.6
Weight (lbs)	2373	2622	2800

Table 11: Wingbox Weight: Multiphase Composites Upper Skin, PZT-5A - Carbon - LaRC-SI 0.2 Aspect Ratio

Volume Fraction	50%	60%	70%
Weight (lbs)	2373	2457	2541

The take-off weight formulation and empty weight fraction from Equation (14) and Equation (16) are applied to determine the empty weight and take-off weight for the modified aircraft. The procedure in Subsection 3.3 is used to determine the weight breakdown of the aircraft with different wingbox upper skin material. Initially, the weight breakdown of the original aircraft is calculated. Based on [61], the original aircraft  $W_{TO}$  is 170000 lbs with 41000 lbs fuel weight. Utilizing Equation (16), 84183 lbs of empty weight is obtained. Thus, 44817 lbs of payload plus crew weight are found.

Table 12 depicted the take-off weight and empty weight for the wingbox with different bulk piezoelectric material. The wingbox weight with various com-

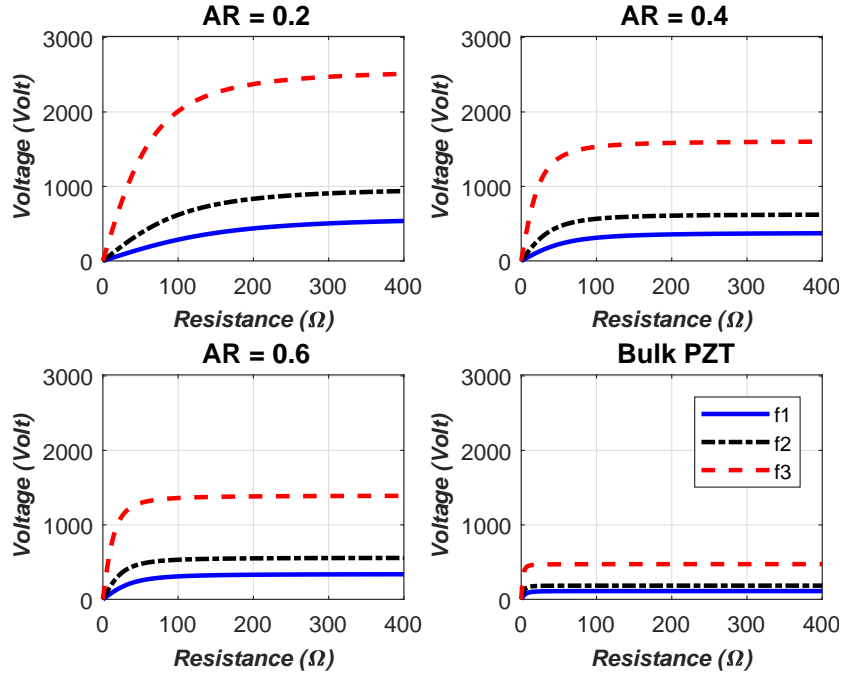


Figure 19: Variation of Voltage Amplitude to The Resistance Load For Wingbox with Multiphase Composite Skin, Aspect Ratio 0.2, 0.4 & 0.6 at 50% Volume Fraction and Bulk PZT Skin

position of multiphase composite as the upper skin are shown in Tables 13 and 14. It can be seen in Table 12 the maximum aircraft empty weight and take-off weight obtained with bulk piezoelectric materials. Meanwhile, the minimum weight is given by the aircraft with the smallest volume fraction and aspect ratio multiphase composite, 50% Vf and 0.2 AR.

Table 12: Aircraft Empty Weight and Take-Off Weight: Different Wingbox Upper Skin Material

Material	Al-2219 [25]	M1832 [25]	PZT-5A
$W_E$ (lbs)	84183	87553	87211
$W_{TO}$ (lbs)	170000	177250	176513

Table 13: Aircraft Empty Weight and Take-Off Weight: Multiphase Composite Wingbox Upper Skin, PZT-5A - Carbon - LaRC-SI 50% Volume Fraction

Aspect Ratio	0.2	0.4	0.6
$W_E$ (lbs)	84099	84597	84593
$W_{TO}$ (lbs)	169820	170890	171656

The modal analysis of the aircraft wingbox is performed prior to the dynamic forced excitation analysis. The natural frequencies are essential to determine the excitation frequencies to be used in the dynamic response analysis. As explained previously, the excitation frequencies lower than the 1st bending natu-

Table 14: Aircraft Empty Weight and Take-Off Weight: Multiphase Composite Wingbox Upper Skin, PZT-5A - Carbon - LaRC-SI 0.2 Aspect Ratio

Volume Fraction	50%	60%	70%
$W_E$ (lbs)	84099	84267	84435
$W_{TO}$ (lbs)	169820	170181	170542

ral frequency are used. The low excitation frequencies are considered more likely to occur for a typical civil jet transport aircraft during cruise load. The 1st bending natural frequencies obtained for different multiphase composite compositions are shown in Table 15.

Table 15: 1st Bending Natural Frequency of The Wingbox for Different Multiphase Composite Composition

Vf	AR	Natural frequency (Hz)
0.5	0.2	2.21
0.5	0.4	1.99
0.5	0.6	1.76
0.6	0.2	2.32
0.7	0.2	2.35
Bulk	PZT-5A	1.61

It can be seen that from Table 15, the 1st bending natural frequencies obtained are quite low, around 1.6-2.3 Hz. The frequency ratio defined in Subsection

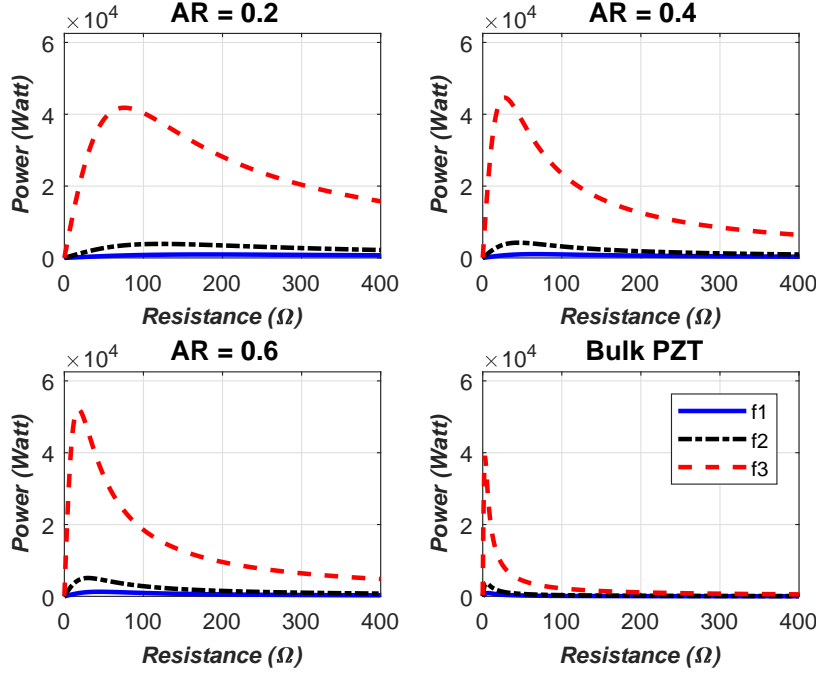


Figure 20: Variation of Power Amplitude to The Resistance Load For Wingbox with Multiphase Composite Skin, Aspect Ratio 0.2, 0.4 & 0.6 at 50% Volume Fraction and Bulk PZT Skin

4.2.2 is used. The dynamic response analysis is performed with 0.5, 0.7, 0.9 frequency ratios as the excitation frequencies. The lift cruise and a unit of moment are used as the actual and dummy loads for the energy harvesting purposes. The procedure explained in Subsection 3.2 is used to determine the voltage and power amplitudes harvested from the cruise load.

The voltage amplitude responses for wingbox with bulk PZT-5A and the multiphase composites at 50% volume fraction are shown in Figure 19. The excitation frequencies denoted by "f1", "f2" and "f3" are 0.2, 0.4, 0.6 frequency ratio, respectively. The voltage responses initially increase with the resistance load until it undergoes an asymptotic behavior at a certain point. The voltage is almost insensitive to the resistance load started from this point. This pattern is aligned with the results displayed in [25].

It is observed that the wingbox with bulk PZT-5A undergoes the asymptotic behavior at the smallest resistance load compared to the multiphase composites. Meanwhile, the wingbox with the multiphase composite at 50% volume fraction and 0.2 aspect ratio undergoes the asymptotic behavior at the largest resistance load. Despite the fact that by increasing the aspect ratio, the PZT-5A fraction increases and larger piezoelectric coupling is obtained, it goes asymptotic at smaller resistance, hence the achieved maximum voltage is smaller. In addition, it is seen, the largest

excitation frequency exerted the highest level of the maximum voltage as it gives the highest displacement amplitude.

In Figure 20, the power amplitude response for wingbox with bulk PZT-5A and the multiphase composites at 50% volume fraction are depicted. The power responses initially increase with the resistance load until a maximum point before declining. The maximum power response is obtained at the first resistance load before the voltage response becomes asymptotic. This trend is also aligned with the pattern observed in [25]. It is interesting to highlight that the maximum power of all the multiphase composites, including the bulk PZT-5A, are around the same level, 40-50 kW, at 0.9 frequency ratio excitation. This phenomenon is considered a positive insight for the weight-energy evaluation as the multiphase composites are lighter than the bulk PZT.

Figure 20 shows the optimum power is varied in a small range of resistance loads, around tens  $\Omega$ . The wingbox with bulk PZT achieved the maximum power at the smallest resistance load as it is the earliest to reach the asymptotic voltage. The wingbox with multiphase composite at 50% volume fraction and 0.2 aspect ratio obtained the maximum power at the largest resistance load compare to the other compositions. However, it is important to notice; the power is dropped significantly outside the optimum

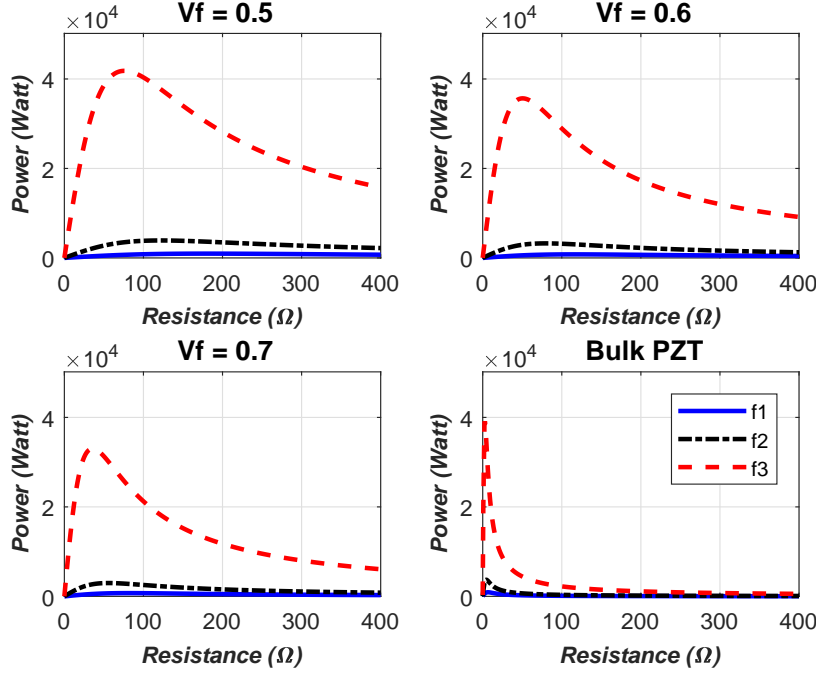


Figure 21: Variation of Power Amplitude to The Resistance Load For Wingbox with Multiphase Composite Skin, Volume Fraction 50%, 60% & 70% at 0.2 Aspect Ratio and Bulk PZT Skin

power range. Therefore, apart from the structural composition, the selection of the resistance loads is one of the key parameters to construct an optimum harvester design.

Table 16: Maximum Power Amplitude and Resistance Load at Maximum Power of The Wingbox for Different Multiphase Composite Composition with 0.9 Frequency Ratio Excitation

Vf	AR	Max Power (kW)	R ( $\Omega$ )
0.5	0.2	41.82	75.92
0.5	0.4	44.64	27.69
0.5	0.6	52.09	17.74
0.6	0.2	35.67	50.43
0.7	0.2	33.02	35.72
Bulk	PZT-5A	39.13	2.73

Moreover, the power amplitude response for wingbox with bulk PZT-5A and the multiphase composites at 0.2 aspect ratio and different volume fraction are depicted in Figure 21. The level of maximum power decreases as the volume fraction increases. The composite is stiffer at longitudinal/fiber direction with higher volume fraction. Hence, it resulted in a smaller displacement level, as well as lower level of voltage/power harvested. In more details, the maximum power and the resistance load at maximum power for the wingbox with the various multiphase composition are shown in Table 16.

## 6. Aircraft Fuel Saving Evaluation

In this section, the power responses obtained from the energy harvesting simulation as presented in Section 5 are evaluated against the weight change of the aircraft. In the present work, the power responses are equivalenced with the fuel used for Auxiliary Power Unit (APU) operation. The procedure explained in Subsection 3.3 is applied.

The APU for long-range civil jet aircraft, i.e., the Airbus A320 or the Boeing 737, is used as a comparison. The APU generator can supply the aircraft normal electrical loads and taxiing system, around 90kW, with the 2kg/min fuel consumption [63, 64]. Thus, for 1-hour operation, the APU produces 324 Mega-Joule energy with 264.5 lbs fuel consumed or 1220 kilo-Joule per pound fuel. Based on this data, the equivalent fuel saving from the power harvested is calculated.

Table 17: Aircraft Fuel Saving Evaluation: Wingbox with Piezoelectric Upper Skin in [25]

$\Delta W_{fuel-Str}$ (lbs)	$P_{Ave}$ (kW)	$\Delta W_{fuel-Pwr}$ (lbs)	<b>TOTAL</b> $\Delta W_{fuel}$ (lbs)
<b>+3880</b>	25.24	<b>-148</b>	<b>+3732</b>

Note: +/- shows fuel addition/reduction to the original fuel weight

Table 18: Aircraft Fuel Saving Evaluation: Wingbox with Bulk PZT-5A Upper Skin

$fr$	$\Delta W_{fuel-Str}$ Structural (lbs)	$P_{Ave}$ (kW)	$\Delta W_{fuel-Pwr}$ Power (lbs)	<b>TOTAL</b> $\Delta W_{fuel}$ (lbs)
0.5	+3485	0.92	- 2	+3483
0.7	+3485	3.72	- 12	+3473
0.9	+3485	39.1	-167	+3318

Table 19: Aircraft Fuel Saving Evaluation: Wingbox with PZT-5A - Carbon - LaRC-SI Composite Upper Skin

Vf	AR	$fr$	$\Delta W_{fuel-Str}$ (lbs)	$P_{Ave}$ (kW)	$\Delta W_{fuel-Pwr}$ (lbs)	<b>TOTAL</b> $\Delta W_{fuel}$ (lbs)
		0.5	- 96	0.96	- 3	- 99
50%	0.2	0.7	- 96	3.90	- 18	-114
		0.9	- 96	41.8	-244	-340
		0.5	+476	1.05	- 3	+473
50%	0.4	0.7	+476	4.24	- 17	+362
		0.9	+476	44.6	-235	+241
		0.5	+886	1.28	- 3	+883
50%	0.6	0.7	+886	5.26	- 18	+868
		0.9	+886	52.1	-242	+644
		0.5	+ 97	0.79	- 3	+ 94
60%	0.2	0.7	+ 97	3.25	- 16	+ 81
		0.9	+ 97	35.7	-219	-122
		0.5	+290	0.72	- 3	+287
70%	0.2	0.7	+290	2.98	- 14	+276
		0.9	+290	33.0	-205	+ 85

Table 17 depicted the fuel weight - energy harvested evaluation for the wingbox in [25]. The " $\Delta W_{fuel-Str}$ " and " $\Delta W_{fuel-Pwr}$ " represent the change of the fuel required due to the change in structural weight and the equivalent of fuel saving from the power harvested. The positive/negative (+/-) signs show the addition/reduction compare to the original fuel weight of all Al-2219 aircraft. The average power harvested from two wingboxes is denoted by " $P_{Ave}$ ".

The " $\Delta W_{fuel-Pwr}$ " is always negative as it is equivalent to the fuel saving. The " $\Delta W_{fuel-Str}$ " can be positive or negative depends on whether the aircraft structure is heavier or lighter. Hence, the total change of the fuel weight, "TOTAL  $\Delta W_{fuel}$ ", can be positive or negative depends on whether the change due to the structure is more or less than the equivalent fuel saving from the power harvested.

It can be seen in Table 17, additional fuel as large as 3700 lbs is required due to the aircraft structure is much heavier when the wingbox upper skin is replaced by bulk piezoelectric, M1832. Although 25 kW of power harvested seems promising, eventually

it is only equivalent to 148 lbs fuel reduction. It is on a much lower scale compared to the structural change which resulted in almost 3900 lbs addition. Similar changes also occur when the wingbox upper skin is replaced by bulk PZT-5A as shown in Table 18.

As depicted in Table 18, the additional fuel required due to structural change is almost 3500 lbs. In total, the extra fuel of around 3300-3500 lbs is needed due to the wingbox upper skin with bulk PZT-5A is heavier than the all Al-2219 wingbox. Even with the excitation load of 0.9 frequency ratio, the equivalent fuel saving from the power harvested is not able to overcome the structural change. However, the structural weight is reduced significantly by replacing bulk PZT-5A with the multiphase composite. The fuel saving evaluation by applying the multiphase composite is depicted in Table 19.

It is seen in Table 19 that the fuel weight due to the structural change is significantly reduced. The maximum total fuel saved is obtained by applying the composite with 50% volume fraction and 0.2 aspect ratio. The aircraft weight is lighter compared to the original

Table 20: Power Density Comparison from Different Case Studies

Case Study	Flight/ Load Condition	Aircraft/Wing Structure	Piezoelectric Structure	Power Density kW/m <sup>3</sup>
Anton & Inman [5]	Flight test, 6 min cruise, V=12.5 m/s, h=30m	RC Aircraft, 1.8m span, 23cm chord	MFC & PFC patches: (102×16×0.3)mm <sup>3</sup> , (145×15×0.3)mm <sup>3</sup>	0.001 (MFC) 0.008 (PFC)
Wang & Inman [14]	Numerical, V=15m/s, Assumed clear sky with 0.02g RMS vibration	Plate-like wing 700.5mm halfspan, 38mm chord	1 Packaged PZT-5A layer (45×25.4×0.5)mm <sup>3</sup>	0.275
Tsushima & Su [23]	Numerical model, Dryden gust, Vg=30m/s, 10s, V=70m/s, h=15km	Tapered Wing, 200cm halfspan, 15cm meanchord	Piezo layers cover upper-lower surfaces, thickness=0.127mm	1.75
Erturk et al. [9]	Wind tunnel test, 25s flutter, V=9.3m/s (critical flutter speed)	2DoF Wing Section, 0.5m span, 25cm chord	Bimorph, Packaged PZT-5A 2×(45×25.4×0.5)mm <sup>3</sup>	4.61
De Marqui Jr. et al. [11]	Numerical Model, 1.5s flutter, V=41m/s (critical flutter speed)	Plate-like wing, 1.2m halfspan 24cm meanchord	Bimorph, PZT-5A 2×(360×240×0.5)mm <sup>3</sup>	8.68
Tsushima & Su [24]	Numerical model, LCO, V=89.25m/s (post-flutter speed)	Tapered Wing, 200cm halfspan, 15cm meanchord	Piezo layers cover upper-lower surfaces, thickness=0.127mm	75.62
Present Work	Hybrid scheme, Dynamic Cruise, L=W <sub>TO</sub> , f=1.99Hz	Jet Aircraft Wingbox, 14.5m halfspan 1.6m meanchord	Multiphase composite as the upper skin (14.5×1.6×0.006)m <sup>3</sup>	147.75
Xiang et al. [20]	Mathematical model, 1-cos gust, Vg=0.15V, 1.05s, V=9.3m/s, h=4km	Tapered Wing, 1m halfspan, 19cm meanchord	1 layer PZT-5H at upper skin (100×40×0.255)mm <sup>3</sup>	251.77

aircraft. Thus, the fuel weight is reduced by almost 100 lbs due to the structural change. Moreover, the equivalent fuel saving around 240 lbs is achievable from the power harvested at 0.9 frequency ratio (2.0 Hz) excitation. Therefore, in total 340 pounds of fuel is saved by applying this multiphase composite composition. In this case, the entire fuel saved is more than the fuel required for 1 hour APU operation.

In general, large volume fraction and aspect ratio is not beneficial for fuel saving. The composite with 50% volume fraction and 0.6 aspect ratio resulted in the heaviest structure increment and the most fuel required amongst other compositions. However, larger volume fraction with small aspect ratio may overcome the additional fuel weight due to structural change.

The composite with 60% volume fraction and 0.2 aspect ratio at 0.9 frequency ratio (2.1 Hz) excitation harvested the power that overcame the structural change. In total, 120 lbs of fuel are saved with this composition or around 45% of the fuel for APU oper-

ation. The larger volume fraction may be beneficial in terms the structural strength. However, the weight - energy - strength evaluation yet to be investigated further.

A comparison with the result from the references is depicted in Table 20. The selected cases provided studies on different structural size with different flight/load condition, i.e., gust load, cruise flight, flutter. The maximum RMS or average power densities, power per volume of piezoelectric layer(s), of each case are compared. Table 20 ranked the power density from the lowest to the highest.

The current case study with multiphase composite (AR 0.2, Vf 50%) provides the second highest power density, lies between a gust load case and a post-flutter speed LCO case. Anton and Inman [5] obtained the smallest power density. However, to be noted that at that time, the mathematical/numerical model to estimate/design the energy harvester has not yet been developed. It can be seen that the power

density mostly varies from the order of  $\text{kW}/\text{m}^3$  to  $10^2 \text{ kW}/\text{m}^3$ .

The variations are most likely influenced by the assumption taken to simulate the load acting on the wings. Even different gust types, discrete 1-cosine gust [20] and Dryden gust/turbulence [23] resulted in different scale of power densities. Despite the 1-cosine gust acting at a much lower speed than the Dryden gust, but the power density is more than a hundred times of the Dryden gust case. Moreover, the study in [23] and [24] despite using the same wing structure, due to different loads, i.e., Dryden gust and LCO vibration, different level of power densities are obtained. The vibration amplitude due to the Dryden gust is not constant over the time, however, at the flutter and LCO case, a persistent oscillation is expected.

The differences may also occur due to various resistance load. Despite most of the selected case study used the optimum resistance load, the cases in [23, 24] only applied one resistance value and it is not mentioned whether that was the optimum resistance. The current study provided the only analysis with a forced excitation load case. A harmonic lift force is assumed with an excitation near the 1st bending frequency. It is important to note that at a cruise flight, the excitation frequency may vary and analysis on different frequencies is required as shown in Tables 18 and 19. Nevertheless, the current study provides a new option to estimate the potential of energy harvesting from large wing structure with the multiphase composite.

In addition, considering overall flight performance, i.e., range, it is found that the current fuel saved still unable to provide significant improvement. For instance, a conceptual mission profile analysis on the original aircraft and the modified one with multiphase composites (AR 0.2, Vf 50%) is performed.

The typical jet transport aircraft mission profile with the weight fraction of each phase is shown in Figure 22. As  $W_{TO}$  is known and  $W_5$  is assumed as the operational empty weight with 5% reserved fuel, hence  $W_2$  and  $W_3$  can be calculated. The range at cruise phase is evaluated using the Breguet's formula [54]. Without energy harvesting activated for the modified aircraft, the range is assumed the same for both aircraft, as well as their velocity, specific fuel consumption, and lift to drag ratio. Thus, the range proportional to  $\ln(W_2/W_3)$  for each aircraft. The fuel consumed during landing & taxiing is found around 390 lbs and  $\ln(W_2/W_3) = 0.197$ .

If the energy harvesting ability is activated and the harvested power is used to support taxiing system, then the equivalent fuel saved from the harvested power, i.e. 244 lbs, can be used to extend the cruise range as shown in Figure 23. The extended range is proportional to  $\ln(W_3/W_3^*)$ . It is calculated that  $\ln(W_3/W_3^*) = 1.84 \times 10^{-3}$ , hence it is found the extended range is only 0.93% of the original range.

If a 3000 km range of cruise is considered, then less than 30 km of extended range is achieved with the energy harvesting ability. Therefore, from this case, the harvested power is not providing a significant impact on the overall flight performance. However, in the airline point of view, more than 200 lbs of fuel saved can be seen as a reduced cost or at least one additional passenger per flight. A comprehensive analysis of the economic side of the operation, i.e., the trade-off between the investment for the enhanced system and the reduced cost/ increased profit, is required in this case.

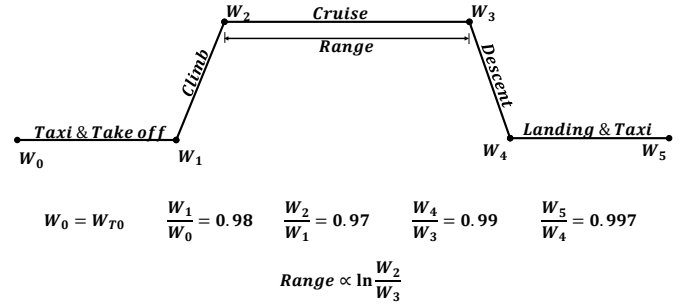


Figure 22: Mission profile of a typical jet transport aircraft

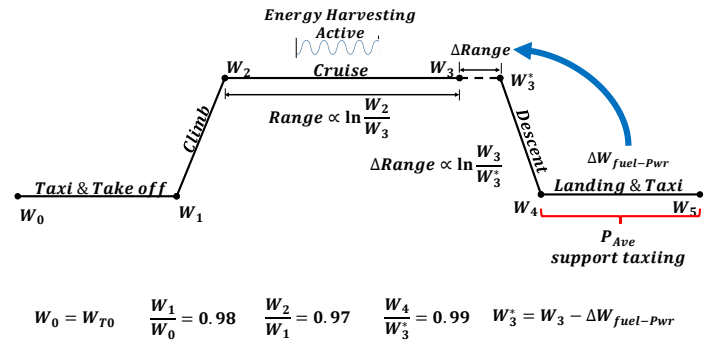


Figure 23: Mission profile with energy harvesting system and extended cruise range using the fuel saved

## 7. Conclusion

A new investigation on the implementation of the multiphase composite application for energy harvesting purpose has been conducted. A computational code based on The Double-Inclusion model combined with Mori-Tanaka method to estimate the effective electro-elastic properties of the multiphase composite has been developed. The capabilities of the present code are shown by comparison with the analytical, experimental and finite element results.

The hybrid FEM/analytical model has been implemented to perform energy harvesting simulation of a notional civil jet aircraft wingbox. The multiphase composites with various compositions have been applied the wingbox upper skin. A new procedure to investigate the trade-off between the aircraft weight, the fuel saved and the harvested energy has been developed. Based on the simulation results, a promising range of the power responses, within 30-50 kW, is achievable. The equivalent of 340 pounds fuel saving is attainable from the power harvested. The fuel saved is more than enough for 1 hour APU operation.

The new procedure proposed is beneficial in terms of the aircraft design process. This method provides a cheap and fast way to establish the sense of the energy harvester design for the aircraft structure. However, some issues are yet to be observed in order to obtain more realistic results. As safety is one of the vital points in aircraft operation, the investigation on the strength of the structure is essential. The optimization of the strength, the energy harvested and the fuel saved need to be explored. Furthermore, a more realistic load is yet to be considered. During flight operation, the aircraft is known to have self-excited aerodynamic loads and gust loads. In this case, an aeroelastic approach may be required.

In addition, higher fidelity computational methods, i.e., a sophisticated micromechanics Representative Volume Element (RVE) model [65] or the multiscale approach [66], may also be considered for further validation/virtual testing of the effective electro-elastic properties. In the present work, a rather conventional approach to arrange a detailed 3D model of the composite in a row has been performed. On a larger scale, in which a ply composite may consist thousands of fiber, the multiscale approach is more efficient and more established. However, a multiscale approach with a fully coupled electro-mechanical model for energy harvesting purpose is yet to be developed.

## Acknowledgements

The authors gratefully acknowledge the support of Indonesia Endowment Fund for Education (LPDP).

## References

- [1] Christodoulou L, Venables JD. Multifunctional material systems: The first generation. *JOM* 2003;55(12):39–45.
- [2] Gibson RF. A review of recent research on mechanics of multifunctional composite materials and structures. *Compos Struct* 2010;92(12):2793–810.
- [3] Ferreira ADB, Nvoa PR, Marques AT. Multifunctional material systems: A state-of-the-art review. *Compos Struct* 2016;151:3–35.
- [4] Toprak A, Tigli O. Piezoelectric energy harvesting: State-of-the-art and challenges. *Appl Phys Rev* 2014;1(3):031104.
- [5] Anton SR, Inman DJ. Vibration energy harvesting for unmanned aerial vehicles. *Proc SPIE Act Passiv Smart Struct Integr Syst* 2008;6928:692824.
- [6] Erturk A, Inman DJ. Issues in mathematical modeling of piezoelectric energy harvesters. *Smart Mater Struct* 2008;17(6):065016.
- [7] Erturk A, Inman DJ. A distributed parameter electromechanical model for cantilevered piezoelectric energy harvesters. *J Vib Acoust* 2008;130(4):041002.
- [8] Erturk A, Inman DJ. An experimentally validated bimorph cantilever model for piezoelectric energy harvesting from base excitations. *Smart Mater Struct* 2009;18(2):025009.
- [9] Erturk A, Vieira WGR, De Marqui Jr. C, Inman DJ. On the energy harvesting potential of piezoaeroelastic systems. *Appl Phys Lett* 2010;96(18):184103.
- [10] Dias JAC, De Marqui Jr. C, Erturk A. Three-degree-of-freedom hybrid piezoelectric-inductive aeroelastic energy harvester exploiting a control surface. *AIAA J* 2015;53(2):394–404.
- [11] De Marqui Jr. C, Erturk A, Inman DJ. Piezoaeroelastic modeling and analysis of a generator wing with continuous and segmented electrodes. *J Intell Mater Syst Struct* 2010;21(10):983–93.
- [12] De Marqui Jr. C, Vieira WGR, Erturk A, Inman DJ. Modeling and analysis of piezoelectric energy harvesting from aeroelastic vibrations using the Doublet-Lattice Method. *J Vib Acoust* 2011;133(1):011003.
- [13] De Marqui Jr. C, Erturk A. Electroaeroelastic analysis of airfoil-based wind energy harvesting using piezoelectric transduction and electromagnetic induction. *J Intell Mater Syst Struct* 2013;24(7):846–54.
- [14] Wang Y, Inman DJ. Simultaneous energy harvesting and gust alleviation for a multifunctional composite wing spar using reduced energy control via piezoceramics. *J Compos Mater* 2013;47(1):125–46.
- [15] Abdelkefi A. Aeroelastic energy harvesting: A review. *Int J Eng Sci* 2016;100:112–35.
- [16] Li D, Wu Y, Ronch AD, Xiang J. Energy harvesting by means of flow-induced vibrations on aerospace vehicles. *Prog Aerosp Sci* 2016;86:28–62.

- [17] Rostami AB, Armandei M. Renewable energy harvesting by vortex-induced motions: Review and benchmarking of technologies. *Renew Sust Energ Rev* 2017;70:193 – 214.
- [18] Wei C, Jing X. A comprehensive review on vibration energy harvesting: Modelling and realization. *Renew Sust Energ Rev* 2017;74:1 – 18.
- [19] De Marqui Jr. C, Maria MJ. Effect of piezoelectric energy harvesting on the response of a generator wing to a turbulence gust. In: 27th Congress of The International Council of The Aeronautical Sciences. 2010,.
- [20] Xiang J, Wu Y, Li D. Energy harvesting from the discrete gust response of a piezoaeroelastic wing: Modeling and performance evaluation. *J Sound Vib* 2015;343:176–93.
- [21] Bruni C, Gibert J, Frulla G, Cestino E, Marzocca P. Energy harvesting from aeroelastic vibrations induced by discrete gust loads. *J Intel Mat Syst Str* 2017;28(1):47–62.
- [22] Tsushima N, Su W. Modeling of highly flexible multifunctional wings for energy harvesting. *J Aircraft* 2016;53(4):1033–44.
- [23] Tsushima N, Su W. Concurrent active piezoelectric control and energy harvesting of highly flexible multifunctional wings. *J Aircraft* 2017;54(2):724–36.
- [24] Tsushima N, Su W. Flutter suppression for highly flexible wings using passive and active piezoelectric effects. *Aerosp Sci Technol* 2017;65:78 – 89.
- [25] Akbar M, Curiel-Sosa JL. Piezoelectric energy harvester composite under dynamic bending with implementation to aircraft wingbox structure. *Compos Struct* 2016;153:193 – 203.
- [26] Akbar M, Curiel-Sosa JL. Evaluation of piezoelectric energy harvester under dynamic bending by means of hybrid mathematical/isogeometric analysis. *Int J Mech Mater Des* 2017,.
- [27] Thai CH, Nguyen-Xuan H, Nguyen-Thanh N, Le TH, Nguyen-Thoi T, Rabczuk T. Static, free vibration, and buckling analysis of laminated composite Reissner-Mindlin plates using NURBS-based isogeometric approach. *Int J Numer Methods Engrg* 2012;91(6):571–603.
- [28] Curiel Sosa JL, Gil A. Analysis of a continuum-based beam element in the framework of explicit-FEM. *Finite Elem Anal Des* 2009;45(89):583 –91.
- [29] Lin Y, Sodano HA. A double inclusion model for multiphase piezoelectric composites. *Smart Mater Struct* 2010;19(3):035003.
- [30] Lin Y, Sodano HA. Concept and model of a piezoelectric structural fiber for multifunctional composites. *Compos Sci Technol* 2008;68(7):1911 –8.
- [31] Lin Y, Sodano HA. Fabrication and electromechanical characterization of a piezoelectric structural fiber for multifunctional composites. *Adv Func Mater* 2009;19(4):592–8.
- [32] Lin Y, Sodano HA. Electromechanical characterization of a active structural fiber lamina for multifunctional composites. *Compos Sci Technol* 2009;69(11):1825 –30.
- [33] Hori M, Nemat-Nasser S. Double-inclusion model and overall moduli of multi-phase composites. *Mech Mater* 1993;14(3):189 – 206.
- [34] Dunn ML, Ledbetter H. Elastic moduli of composites reinforced by multiphase particles. *J Appl Mech* 1995;62(4):1023–8.
- [35] Dunn ML, Taya M. An analysis of piezoelectric composite materials containing ellipsoidal inhomogeneities. *Proc R Soc Lond A* 1993;443(1918):265–87.
- [36] Eshelby J. The determination of the field of an ellipsoidal inclusion and related problems. *Proc R Soc Lond* 1957;241:376–96.
- [37] Hashin Z. The elastic moduli of heterogeneous materials. *J Appl Mech* 1962;29:143 –50.
- [38] Mori T, Tanaka K. Average stress in matrix and average elastic energy of materials with misfitting inclusions. *Acta Metall* 1973;21(5):571 –4.
- [39] Abdullah NA, Curiel-Sosa JL, Akbar M. Aeroelastic assessment of cracked composite plate by means of fully coupled finite element and doublet lattice method. *Compos Struct* 2018,.
- [40] Chan HLW, Unsworth J. Simple model for piezoelectric ceramic/polymer 1-3 composites used in ultrasonic transducer applications. *IEEE T Ultrason Ferr* 1989;36(4):434–41.
- [41] Dunn ML, Taya M. Micromechanics predictions of the effective electroelastic moduli of piezoelectric composites. *Int J Solids Struct* 1993;30(2):161 –75.
- [42] Odegard G. Constitutive modeling of piezoelectric polymer composites. *Acta Mater* 2004;52(18):5315 –30.
- [43] Hashemi R, Weng G, Kargarnovin M, Shodja H. Piezoelectric composites with periodic multi-coated inhomogeneities. *Int J Solids Struct* 2010;47(21):2893 –904.
- [44] Kuo HY. Multicoated elliptic fibrous composites of piezoelectric and piezomagnetic phases. *Int J of Eng Sci* 2011;49(7):561 –75.
- [45] Malakooti MH, Sodano HA. Multi-inclusion modeling of multiphase piezoelectric composites. *Compos Part B Eng* 2013;47:181 –9.
- [46] Li JY, Dunn ML. Micromechanics of magneto-electroelastic composite materials: Average fields and effective behavior. *J Intel Mat Syst Str* 1998;9(6):404–16.
- [47] Dinartz F, Sabar H. Magneto-electro-elastic coated inclusion problem and its application to magnetic-piezoelectric composite materials. *Int J Solids Struct* 2011;48(16):2393 –401.
- [48] Kuo HY, Bhattacharya K. Fibrous composites of piezoelectric and piezomagnetic phases. *Mech Mater* 2013;60:159 –70.
- [49] Zhou K, Hoh HJ, Wang X, Keer LM, Pang JH, Song B, et al. A review of recent works on inclusions. *Mech Mater* 2013;60:144 –58.
- [50] Sairajan K, Aglietti G, Mani K. A review of multifunctional structure technology for aerospace applications. *Acta Astronaut* 2016;120:30 – 42.
- [51] Standards Committee of the IEEE Ultrasonics, Ferroelectrics, and Frequency Control Society . IEEE Standard on Piezoelectricity. ANSI/IEEE Std 176-1987 1988,.
- [52] Li JY. Magneto-electroelastic multi-inclusion and inhomogeneity problems and their applications in composite materials. *Int J of Eng Sci* 2000;38(18):1993 – 2011.
- [53] Mikata Y. Determination of piezoelectric eshelby tensor in transversely isotropic piezoelectric solids. *Int J of Eng Sci* 2000;38(6):605 –41.
- [54] Raymer DP. *Aircraft Design: A Conceptual Approach*. AIAA Education Series; American Institute of Aeronautics and Astronautics, Inc.; 1992. ISBN 0930403517.
- [55] Wagner M, Norris G. *Boeing 787 Dreamliner*. MBI Publishing Company; 2009. ISBN 9781616732271.
- [56] Gohardani O, Elola MC, Elizetxea C. Potential and

prospective implementation of carbon nanotubes on next generation aircraft and space vehicles: A review of current and expected applications in aerospace sciences. *Prog Aerosp Sci* 2014;70:42 – 68.

- [57] De Marqui Jr. C, Erturk A, Inman DJ. An electromechanical finite element model for piezoelectric energy harvester plates. *J Sound Vib* 2009;327(1):9 – 25.
- [58] Kuo HY, Peng CY. Magnetolectricity in coated fibrous composites of piezoelectric and piezomagnetic phases. *Int J of Eng Sci* 2013;62:70 – 83.
- [59] Dinzart F, Sabar H. Electroelastic behavior of piezoelectric composites with coated reinforcements: Micromechanical approach and applications. *Int J Solids Struct* 2009;46(20):3556 –64.
- [60] Koutsawa Y, Belouettar S, Makradi A, Tiem S. X-FEM implementation of VAMUCH: Application to active structural fiber multi-functional composite materials. *Compos Struct* 2012;94(4):1297 –304.
- [61] Ainsworth J, Collier C, Yarrington P, Lucking R, Locke J. Airframe wingbox preliminary design and weight prediction. In: 69th Annual Conference on Mass Properties, Virginia Beach, Virginia. 2010, p. 41.
- [62] Ballas RG. Piezoelectric Multilayer Beam Bending Actuators: Static and Dynamic Behavior and Aspects of Sensor Integration. *Microtechnology and MEMS*; Springer Berlin Heidelberg; 2007. ISBN 9783540326427.
- [63] Yann N. eTAXI Taxiing aircraft with engines stopped. AIRBUS S.A.S.; 2013, p. 2–10.
- [64] Scholz D. An optional APU for passenger aircraft. In: 5th Council of European Aerospace Societies Air and Space Conference: Challenges in European Aerospace, Delft. 2015,.
- [65] Pulungan D, Lubineau G, Yudhanto A, Yaldiz R, Schijve W. Identifying design parameters controlling damage behaviors of continuous fiber-reinforced thermoplastic composites using micromechanics as a virtual testing tool. *Int J Solids Struct* 2017;117:177 –90.
- [66] Molina AC, Curiel-Sosa J. A multiscale finite element technique for nonlinear multi-phase materials. *Finite Elem Anal Des* 2015;94:64 – 80.